Sterile neutrino dark matter from the cosmic QCD epoch

Dissertation

submitted to the

Faculty of Physics, Bielefeld University

by

Alexander Klaus

April 2021

Supervisor and 1st Reviewer:
Prof. Dr. Dietrich Bödeker

2nd Reviewer:
Prof. Dr. Dominik J. Schwarz

Published work

A large portion of results presented in this thesis has been previously published in the following article [1]:
D. Bödeker and A. Klaus,
Sterile neutrino dark matter: impact of active-neutrino opacities,
J. High Energ. Phys. 2020, 218 (2020),
arXiv: 2005.03039 [hep-ph].

Declaration

This thesis has not been previously submitted to any examination office by the author. Only the sources and literature indicated have been used.

Abstract

Dark matter may be comprised of keV-mass sterile neutrinos, which were mainly produced during the Quantum Chromodynamics (QCD) epoch of the early Universe. The production could be strongly affected by opacities (or damping rates) of active neutrinos, which receive non-perturbative QCD contributions. We investigate the importance of these contributions and find that they significantly affect the sterile neutrino yield only in the case of non-resonant production. The latter can however only provide a small fraction of the relic dark matter abundance, since it is subject to strong constraints from X-ray observations of sterile neutrino decay, as well as Lyman-α observations connected to structure formation. In the presence of large lepton asymmetries, the production can be resonantly enhanced and a significant fraction of the dark matter can be produced, while observational constraints are much weaker. In that case however, we find that the yield turns out to be insensitive to changes of the opacities. Thus, non-perturbative QCD contributions to the opacities will not affect this dark matter scenario. Furthermore, we obtain larger sterile neutrino yields than previous studies and thus weaker lower limits on the active-sterile mixing angle from big bang nucleosynthesis. In addition, we calculate lower limits on the mixing angle from the cosmic microwave background, which has not been done before in the context of sterile neutrino dark matter. These limits are weaker than the limits from big bang nucleosynthesis but also more robust due to smaller systematic uncertainties. Finally, we investigate a simple extension of the Standard Model in which a new scalar field, mediating self-interactions among active neutrinos, poses an alternative to large lepton asymmetries in helping to efficiently produce sterile neutrino dark matter. The new scalar field can also lead to resonant production, however its contribution to the active neutrino opacity is much higher than the Standard Model contribution and reduces the significance of resonances. Nevertheless, the available parameter space in which the dark matter abundance can be produced is quite large due to weak observational constraints in this scenario.

Contents

Chapter 1

Introduction

Gaining a deeper understanding of the building blocks that make up the world around us, from the smallest scales on the quantum level to the largest scales of cosmology, often requires the connection of puzzle pieces from opposite sides of this spectrum. On the one side, the advancements in theoretical and experimental particle physics of the last few decades have opened our eyes to a variety of fundamental particles and laws that govern their interplay, collectively forming the Standard Model (SM) of particle physics. On the other side, the Lambda-Cold-Dark-Matter model (ΛCDM) serves as the cosmological standard model that describes the evolution of the Universe as a whole, and is well-founded based on many observations on large scales, like the cosmic microwave background (CMB) or the accelerating expansion of the Universe. What appears to be a separation of different worlds by many orders of magnitude in length and by different forces dictating how the states of a given system evolve, turns out to be deeply connected in many instances. For example, roughly 300.000 years after the Big Bang, when the Universe was much hotter and denser than today, most of the energy density resided in a plasma of relativistic particles. Due to the cosmological expansion, the energy density decreased and the plasma cooled down. Then at some point, the interaction rate of photons with the electrons in the plasma was overtaken by the expansion rate of the Universe, which lead to their decoupling. These photons subsequently streamed freely through spacetime, which marked the birth of the CMB. The discovery of this relic in 1965 [2] teaches us that, in order to make sense of the cosmic evolution from very early on, one needs to have a good idea of the relevant processes on the smallest scales of elementary particles, as described by the SM. The SM has proven its success in numerous experimental tests and searches over the last decades. Most notably, the discovery of the Higgs boson in the Large Hadron Collider at CERN [3, 4] confirmed the theory of spontaneously broken electroweak symmetry and the resulting mass generation for most of the known elementary particles.

A lot of what we know about the current state of the Universe stems from precise

measurements of the CMB. It is highly isotropic, with small temperature fluctuations of the order $\delta T/T \sim 10^{-5}$ after subtracting the dipole anisotropy contributions [5]. The latter come from our own movement through space, as CMB photons coming towards us appear blueshifted and those going away from us appear redshifted. The full-sky map of the CMB is analyzed in terms of a power spectrum of temperature fluctuations, which sensitively depends on the parameters of the cosmological model. The contributions ρ_i to the present energy density coming from dark matter, baryonic matter, dark energy and curvature are parametrized by the respective density parameters $\Omega_i = \rho_i/\rho_c$, where $\rho_c = 3H_0^2/8\pi G$ is the energy density of a spatially flat universe, which is also to very high accuracy the present energy density. Here, $H_0 = (67.4 \pm 0.5)\mathrm{km\,s^{-1}Mpc^{-1}}$ [6] is the current value of the Hubble parameter and G is the gravitational constant. Currently, the most precise estimates of the free parameters of the ΛCDM model are given by the Planck collaboration [6], with best fit results

$$\begin{aligned} \Omega_{\mathrm{DM}} &= 0.265 \pm 0.007, \\ \Omega_{\mathrm{b}} &= 0.0493 \pm 0.0006, \\ \Omega_{\Lambda} &= 0.685 \pm 0.007, \\ \Omega_K &= 0.001 \pm 0.002, \end{aligned} \tag{1.1}$$

for the contributions to the present energy density coming from dark matter, baryonic matter, dark energy and curvature. Astonishingly, about 85% of the energy content subscribed to non-relativistic matter is dark matter, of which we know nothing about its composition. We know that it is responsible for various gravitational phenomena that cannot be explained just by the amount of luminous matter and with our current theory of gravity, General Relativity. Most existing theories assume that it is composed of one or more yet unknown particle species, which must have been produced during an early stage of the Universe. In any case, the SM of particle physics does not provide an explanation.

Assuming that after their production, these dark matter particles were in thermal equilibrium with the SM particles in the early Universe, they must have decoupled at some point and then continued to stream freely. Depending on their mass M and the decoupling temperature T_{dec}, one usually distinguishes between cold, warm and hot dark matter. If $T_{\mathrm{dec}} \ll M$, the particles are non-relativistic when they decouple and thus referred to as *cold*. In the opposite case, $T_{\mathrm{dec}} \gg M$, they are still highly relativistic upon decoupling and referred to as *hot*. Finally, the particles can be considered *warm* as an intermediate in between those two extremes. Cosmologies with purely cold dark matter, as described by the ΛCDM model, seem to be conflicting with observed structures on small scales, as they generally predict a more efficient structure formation than what is required to match observations. Prime examples are the missing-satellite problem [7] and the too-big-to-fail problem [8]. On the flip

side, purely hot dark matter prevents the formation of structures like galaxies and galaxy clusters [9]. This excludes for example SM neutrinos as the sole dark matter constituent. Warm dark matter could be a way out, as it allows for the formation of larger structures and simultaneously reduces the build-up of smaller ones [10].

The main actor of this thesis is the sterile neutrino, a hypothetical particle that may serve as a candidate for warm dark matter if its mass lies in the keV-range. A sterile neutrino is quite similar to the SM neutrino, only that it is right-handed and therefore does not take part in weak interactions, which justifies the term *sterile*. In contrast, the SM neutrino is then usually referred to as an *active* neutrino. The extension of the SM by right-handed neutrinos is theoretically very well motivated. They may not only serve as a dark matter candidate but also provide non-zero masses for the active neutrinos and explain active-neutrino oscillations. Furthermore, they might play a key role in the generation of the matter-antimatter asymmetry of the Universe. However, these possibilities typically require sterile neutrinos on very different mass scales and are difficult to be realized simultaneously, see section 3.1.

The minimal extension of the SM by one family of sterile neutrinos can explain the origin of dark matter. The simplest scenario is the production of sterile neutrino dark matter via active-sterile oscillations in the early Universe. This scenario was originally proposed by Dodelson and Widrow [11], but was later disfavored by strong observational constraints on the sterile neutrino mass and mixing angle [12–14]. One way to circumvent these constraints was suggested by Shi and Fuller [15]. They assumed the presence of primordial lepton asymmetries, much larger than the observed baryon asymmetry. These lead to resonant production of sterile neutrinos, with qualitative differences to the Dodelson-Widrow scenario that greatly weaken the parameter constraints and thus make sterile neutrino dark matter feasible. A crucial feature of these active-sterile mixing scenarios is that the production of keV-mass sterile neutrinos is most effective for temperatures $T \sim \mathcal{O}(100)\,\mathrm{MeV}$ [11, 16–19]. More specifically, in their original work, Dodelson and Widrow give the maximal production temperature [11]

$$T_{\max} \sim 133\,\mathrm{MeV}\left(\frac{M}{\mathrm{keV}}\right)^{\frac{1}{3}}, \tag{1.2}$$

where M denotes the sterile neutrino mass. For $M \sim \mathcal{O}(\mathrm{keV})$, we find ourselves in the epoch where the strong interaction, as described by Quantum Chromodynamics (QCD), has a large coupling and is generally non-perturbative. During this epoch, the plasma of strongly interacting quarks and gluons undergoes a smooth crossover [20,21], in which these initially free particles confine into hadrons as the temperature drops. Since the quarks are also subject to the weak force, the QCD crossover is naturally also relevant for the neutrino sector of the SM, which in turn can have important consequences for sterile neutrino production.

A key ingredient in determining the production rate of sterile neutrino dark matter is the active-neutrino propagator. It is modified by self-energy corrections, coming from interactions with leptons and quarks. The latter naturally come with uncertainties from the QCD epoch. The most difficult to compute are hadronic contributions to the imaginary part of the active neutrino self-energy, or opacity. One goal of this thesis is to answer the question of how important this hadronic opacity contribution is in the context of sterile neutrino production. The case of resonant production is especially interesting as it can provide for the dark matter. Besides resonant sterile neutrino production through large lepton asymmetries, we also investigate a model in which a potential cause of resonances is provided by self-interactions among active neutrinos, mediated by an additional scalar field beyond the SM. This model leads to a rather weakly constrained scenario of sterile neutrino dark matter, in which efficient production is rather easily achieved [22].

The remainder of this thesis is structured as follows: In chapter 2, we briefly review some observations that confirm the dark matter hypothesis and discuss some particle candidates beyond the SM. We also discuss other fundamental problems of the SM, namely neutrino masses and the baryon asymmetry of the Universe. Chapter 3 will serve as an introduction to sterile neutrinos and explain how different variants of this hypothetical particle can solve the different SM problems. The main focus will lie on sterile neutrino dark matter, its properties and constraints on the respective parameters. Furthermore, we introduce non-resonant and resonant production scenarios in the early Universe, as well as further parameter constraints associated with them. Finally, uncertainties related to QCD are introduced. In chapter 4, we introduce evolution equations for the sterile neutrino phase space densities and lepton number densities and investigate the various leptonic and hadronic contributions entering through the active-neutrino propagator. In chapter 5, we present numerical solutions of the evolution equations and work out the influence of active-neutrino opacities on non-resonant and resonant sterile neutrino production. Based on our findings, we are able to update the lower limit on the active-sterile mixing angle in chapter 6 and extend the viable parameter space for the resonant production scenario. We also confirm a lower limit on the sterile neutrino mass which is based on observations of the Lyman-α forest and finally, summarize all relevant limits in a new exclusion plot. In chapter 7, we study a model in which the SM is extended by an additional scalar field. We investigate how this influences sterile neutrino production efficiency and the relevance of resonances, which may occur even in the absence of any lepton asymmetries. Chapter 8 summarizes our findings.

Chapter 2

Beyond the Standard Model

In this chapter we shortly review some of the observations that lead to the postulation of the existence of dark matter. We have a look at some of the most popular particle candidates, which immediately takes us beyond the realm of the SM of particle physics. We also shortly discuss other challenges the SM faces, which will then further motivate the introduction of sterile neutrinos in the next chapter.

2.1 Some dark matter phenomenology

The first hint that the Universe holds more matter than what is detected somewhere on the electromagnetic spectrum, was given by Zwicky in 1933 [23]. When studying the Coma cluster, he found that the galaxies in the cluster were moving much faster than expected from the virial theorem. He concluded that the mass density inside the cluster should be at least 400 times higher than the density derived from measurements of the visible matter. A possible explanation would be the presence of a halo of non-visible matter, which he called dark matter, in a much greater abundance than the visible matter. Today we have data from numerous observations on different length scales, which strengthen Zwicky's conclusion and further substantiate the dark matter hypothesis.

2.1.1 Galactic rotation curves

One very prominent example is the measurement of rotational velocities of spiral galaxies. Based on Newtonian dynamics and the assumption that a large proportion of the galaxy's mass is accumulated in some inner region, the velocity of the outer regions is expected to decrease like the inverse square root of the galactic radius,

$$v(r) = \sqrt{\frac{GM(r)}{r}}, \tag{2.1}$$

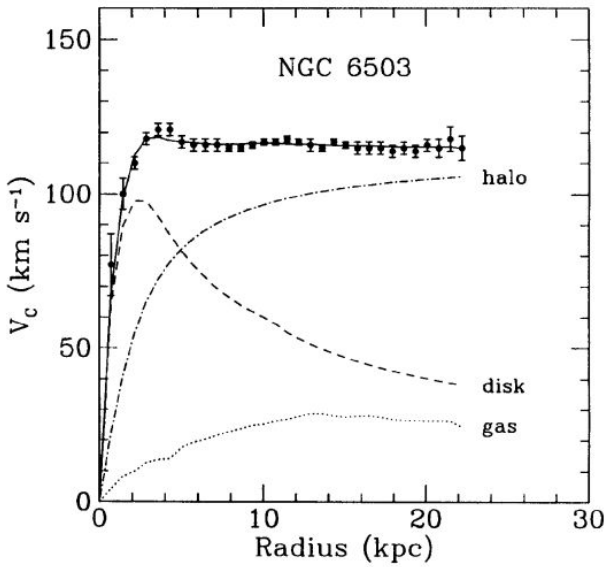

Figure 2.1: Measured values of the rotational velocity of the spiral galaxy NGC 6503 together with the best-fit curve (thick black line). The other three lines are the rotation curves of the individual matter contributions, which together fit the experimental data. The dashed curve is for the disk, the dotted curve for the visible gas and the dash-dotted curve for the dark halo. Taken from [25].

where $M(r)$ is the distribution of the visible matter and G is Newton's gravitational constant. The mass should remain constant for very large radii. However, it was found that the velocity of the outer arms does not slow down with increasing radius, but instead remains nearly constant [24]. An example is shown in figure 2.1. The nearly constant velocity reflects a different mass distribution from the visible one. From eq. (2.1), one concludes that the mass increases linearly for large radial distances, $M(r) \propto r$, reflected by the dash-dotted curve. This hints at the existence of dark matter that is clustering around the galaxy with a density profile $\rho(r) \propto 1/r^2$ for large radial distances.

2.1.2 The Bullet cluster

Another observation favoring the dark matter hypothesis is based on gravitational lensing, an effect that is predicted by General Relativity. It describes how a matter distribution between a distant light source and an observer bends the light's path due to the distortion of space-time in that region. The apparent shape of the source then deviates from the typical shape of objects belonging to the same class as the source, like certain galaxies. By measuring many such galaxies and comparing to the specific source under consideration, one can learn about lensing induced distortions and draw conclusions about the structure of the non-luminous matter distribution [26]. A

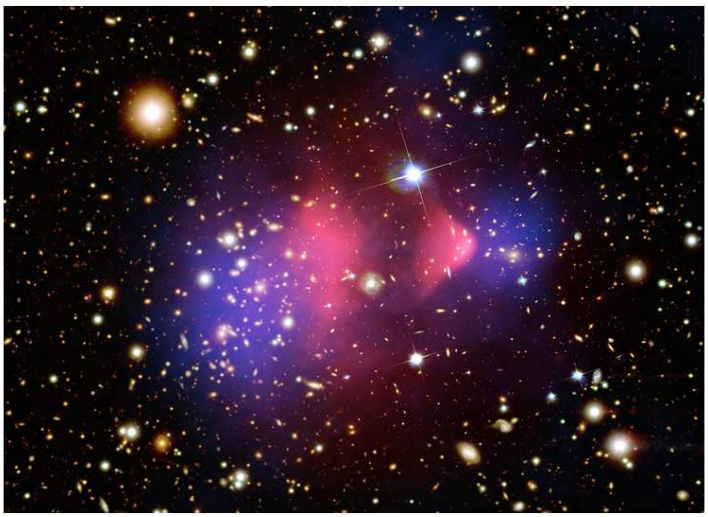

Figure 2.2: Bullet cluster 1E0657-56. This image is an overlay of several observations. The optical image from the Magellan and the Hubble Space Telescope shows galaxies in white and orange. The pink overlay stems from the hot gas as observed by the Chandra X-ray Observatory and represents the bulk of ordinary matter. The blue overlay shows most of the mass, which is dominantly dark, as reconstructed by gravitational lensing. Taken from [29].

famous example in which this mass reconstruction procedure supports the existence of dark matter is the Bullet cluster, a system of two galaxy clusters that collided with each other. It is shown in figure 2.2. Via weak lensing mass reconstruction it was possible to show that most galaxies from both clusters basically passed through each other, which is possible due to their sparse distributions [27]. But X-ray observations have shown that the bulk of the electromagnetically interacting and hot gas, which makes up most of the total visible mass of the system, is left in between both clusters [28]. If the only source of mass was visible matter, we would expect most of it to be distributed in the same way as the hot gas. But the observations tell us that the majority of the mass is centered around the stars in the galaxies, not around the gas. Thus, the major mass component must be dark matter, which behaves mostly collisionless.

2.1.3 The cosmic microwave background

Going further to the cosmological scale, evidence for dark matter is provided by measurements of the CMB. Features of its power spectrum offer a lot of information on the Universe's composition, see ,e.g., [30] for an intuitive review. The impact of dark matter on CMB anisotropies can roughly be summarized as follows. Before

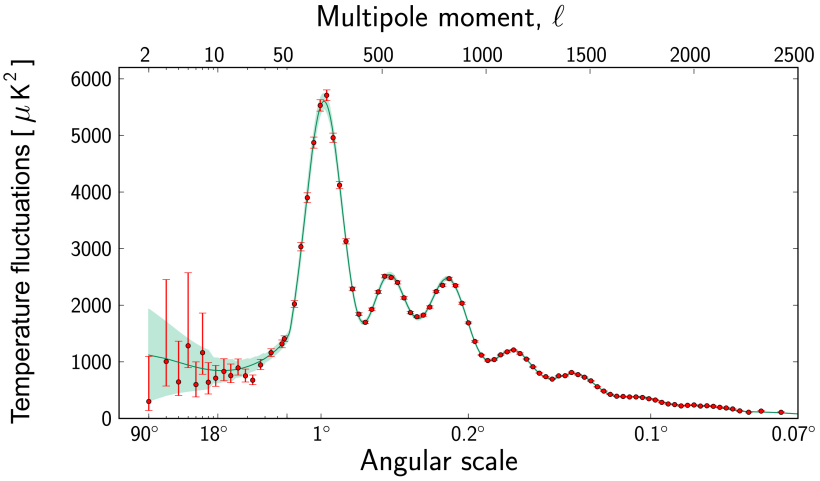

Figure 2.3: Planck power spectrum of temperature fluctuations in the CMB. Red dots with error bars are measured data, the green curve is the best fit to the ΛCDM, the pale green stripe corresponds to predictions of model variations that best agree with the data. Figure taken from [31].

the atoms in the Universe became neutral, the photons were still tightly coupled to the baryonic matter. Due to its collisionless nature, dark matter was able to cluster gravitationally, providing for perturbations in the gravitational potential. These perturbations drove gravitational clusterings in the photon-baryon plasma, which were however counteracted by electromagnetic repulsion. The photon-baryon plasma began to oscillate in and out of overdense regions, the back and forth being due to gravitational pull and radiational push. The phases of these oscillations froze in at the time the photons decoupled from the rest of the plasma and were projected onto the sky as a series of so-called acoustic peaks [5], visible on sub-degree scales ($100 \lesssim l \lesssim 1000$) in the CMB power spectrum, as shown in figure 2.3. The angular scale and height of these peaks are powerful probes of cosmological parameters and the ΛCDM model with the parameters in (1.1) provides an excellent fit [6]. Therefore the CMB power spectrum not only provides very strong evidence for the existence of dark matter, but also precisely predicts its relic abundance.

2.2 Searching for a suitable particle candidate

Assuming that dark matter consists purely of one type of elementary particle, it quickly becomes clear that the search for it must go beyond the SM. Most obviously, the wanted particle must not underly electromagnetic or strong interactions, since

they should lead to observable effects on large scales. Furthermore it must be stable or extremely long lived, with a lifetime exceeding the age of the Universe. This immediately narrows the list of SM candidates down to the neutrinos. However, their tiny masses[1] make them a hot dark matter candidate, which is incompatible with structure formation. They are only allowed to make a small contribution to the dark matter energy density.

We mention that as an alternative to the particle hypothesis, some theories manage to explain some observations not by dark matter but by modifying gravity itself. Modified Newtonian Dynamics (MOND), for example, provides an enhanced gravitational attraction by modifying Newton's force law, leading to a successful prediction of the rotation curves of low-surface-brightness galaxies [32]. On the flip side, theories of modified gravity like MOND are unable to explain the observations from the Bullet cluster. Without dark matter, the dominant mass component of the cluster would be the X-ray gas. The mass peak obtained via weak lensing should then coincide with the gas, which is not the case [27].

There exist many candidates for dark matter, with very different physical backgrounds and we will certainly not be able to give a complete list. Exotic ones may include, e.g., axinos, gravitinos or neutralinos that originate from supersymmetric theories [33], or Kaluza-Klein particles arising from extra dimensional extensions of the SM [34]. Besides candidates on the elementary particle side, there exist various candidates on macroscopic scales. Popular ones include primordial black holes [35] or massive astrophysical compact halo objects (MACHOs) [36], like brown dwarfs, neutron stars or black holes.

There exists a huge variety of dark matter candidates beyond the SM, some of which have been more popular than others in the last decades. In this section, we want to focus on arguably the two most popular particle candidates besides sterile neutrinos, namely WIMPs and axions.

2.2.1 WIMPs

The WIMP (weakly interacting massive particle) might provide the dark matter density via the freeze-out mechanism. Its name actually does not refer to a specific elementary particle, but rather to a broader class of particles. In [37] it was introduced in the form of a heavy right-handed neutrino. In general it is a neutral, stable particle X, which initially resides in thermal equilibrium with the primordial plasma at high temperatures $T \gtrsim m_X$. It constantly undergoes creation and annihilation processes with its coinciding anti-particle $\bar{X}$. Once the temperature drops below its mass, the number density begins to drop due to annihilation processes, which cannot

[1] In the SM, neutrinos are exactly massless, which is a problem on its own and discussed further below.

be balanced by the corresponding creation processes anymore. The evolution of its number density n_X is governed by the Boltzmann equation

$$\frac{dn_X}{dt} = -3Hn_X - \langle\sigma v\rangle\,(n_X^2 - n_{\text{eq}}^2). \tag{2.2}$$

Here H is the Hubble rate, $\langle\sigma v\rangle$ is the thermally-averaged annihilation cross-section and n_{eq} the equilibrium density. The number density initially tracks the equilibrium density. At some point in time, the temperature drops to the freeze-out temperature, a critical value at which the annihilation rate is taken over by the expansion rate and the annihilations stop. Then the number of X-particles in a comoving volume element remains constant, this process is referred to as freeze-out. As an order of magnitude estimate, the solution to (2.2) provides a present relic density [38]

$$\Omega_X h^2 \sim \frac{10^{-27}\text{cm}^3 s^{-1}}{\langle\sigma v\rangle} \sim \frac{10^{-10}\text{GeV}^{-2}}{\langle\sigma v\rangle}. \tag{2.3}$$

Thus, assuming an annihilation cross-section on the weak scale, $\langle\sigma v\rangle \sim 10^{-9}\,\text{GeV}^{-2}$, one obtains a density that is remarkably close to the relic dark matter density $\Omega_{\text{DM}}h^2 \approx 0.12$ [6]. This incidental feature is known as the 'WIMP miracle' and naturally makes the WIMP an attractive candidate for dark matter.

2.2.2 Axions

Another candidate, or rather another class of candidates comprises axions and axion-like particles (ALPs), which typically encompass very light scalar or pseudoscalar fields. The axion is a hypothetical particle originally associated with the Peccei-Quinn symmetry as a solution to the strong CP problem [39]. The SM Lagrangian's main source of CP violation is a phase in the CKM matrix that is needed in the description of quark mixing. However, there is another CP violating term in the QCD sector associated with non-trivial topological configurations of the QCD vacuum,

$$\mathcal{L}_\theta = -\theta\frac{\alpha_s}{8\pi}F^{\mu\nu a}\widetilde{F}_{\mu\nu a}. \tag{2.4}$$

Here, α_s is the fine-structure constant of strong interactions, F is the gluon field-strength tensor and $\widetilde{F}$ its dual. θ is a free parameter of the theory which needs to be determined experimentally. One would argue that most naturally, its value should be of order 1, as there are no theoretical arguments suggesting otherwise. However, measurements of the neutron electric dipole moment pose very stringent bounds, pushing its value down to $\theta \lesssim 10^{-10}$ [40]. This discrepancy is the strong CP problem. Peccei and Quinn proposed the following solution: They consider an additional global $U(1)$ symmetry, which is spontaneously broken and the θ-term

(2.4) is canceled dynamically. The axion a emerges as the Nambu-Goldstone boson associated with the symmetry breaking and it couples to the QCD gauge sector via

$$\mathcal{L} = \frac{a}{f_{PQ}} \frac{\alpha_s}{8\pi} F^{\mu\nu a} \widetilde{F}_{\mu\nu a}, \tag{2.5}$$

where f_{PQ} is the $U(1)$ symmetry-breaking scale. In the phase of broken symmetry, the axion field acquires a vacuum expectation value,

$$\langle a \rangle = \theta f_{PQ}, \tag{2.6}$$

providing a vacuum configuration which leads to the cancellation of (2.4) and thus solving the strong CP problem.

Axion dark matter is a very broad subject, with different possible production scenarios that may underly different parameter constraints. Axions may have been produced thermally in the early Universe via interactions involving quarks and gluons [41], which would contribute a hot dark matter fraction [42]. More attractive is their possible role as cold dark matter, which is mainly produced non-thermally via cosmic string decay [43], domain wall decay [44] or most famously via the misalignment mechanism [45–47]. In the latter, topological fluctuations of the gluon fields explicitly break the Peccei-Quinn symmetry, which then drives the axion field towards the minimum of its potential. This process leads to an excitement of coherent axion field oscillations, which ultimately represent a condensate that builds the cold dark matter. Very light, bosonic dark matter tends to carry imprints of quantum effects to macroscopic scales, which is the reason that this type of dark matter is often referred to as *wave* or *fuzzy* dark matter. A more in-depth review of WIMP and ALP physics including the current status and prospects for experimental searches can be found, e.g., in [5].

2.3 Further challenges

Besides having no good dark matter candidate in its repertoire, the SM also lacks the ability to solve a few other, very fundamental puzzles. The most prominent ones are the existence of neutrino masses and oscillations and the origin of the baryon asymmetry of the Universe. Possible solutions to these unanswered questions also involve the introduction of sterile neutrinos, which is why we briefly discuss them here and thus further motivate the following chapter.

2.3.1 Neutrino masses

The neutrino is the only SM fermion that appears only as a left-handed particle, therefore it remains massless after the spontaneous breaking of electroweak symmetry. What might at first look like a superficial problem of theoretical incompleteness

in some sense, turns out to be a severe problem in the light of neutrino oscillations. In such an oscillation, the flavor content of a neutrino traveling through space changes periodically. The flavor of a neutrino is determined by the accompanying charged lepton in a weak interaction, thus a state $|\nu_\alpha\rangle$ with $\alpha = e, \mu, \tau$ refers to weak interaction eigenstate or flavor eigenstate. A freely propagating neutrino, on the other hand, is in a quantum mechanical superposition of all three flavor eigenstates and exists in a mass eigenstate $|\nu_i\rangle$. These states are related by a unitary matrix U,

$$|\nu_\alpha\rangle = \sum_i U_{\alpha i} |\nu_i\rangle . \tag{2.7}$$

If we now fix the energy E, we can consider the evolution of a mass eigenstate in terms of the distance L the neutrino has traveled,

$$|\nu_i(t, L)\rangle = e^{-i\frac{m_i^2}{2E}L} |\nu_i(0)\rangle , \tag{2.8}$$

where the neutrino is assumed to be ultra-relativistic and to carry momentum $p_i \approx E - m_i^2/2E$. Then the amplitude for detecting a neutrino with flavor β, after a neutrino with initial flavor α has traveled the distance L in time t, reads

$$\langle \nu_\beta(t, L)|\nu_\alpha(0)\rangle = \sum_i U^*_{\beta i} U_{\alpha i} e^{-i\frac{m_i^2}{2E}L}. \tag{2.9}$$

The probability for this event is given by

$$|\, \langle \nu_\beta(t, z)|\nu_\alpha(0)\rangle \,|^2 = \sum_{i,j} U^*_{\beta i} U_{\alpha i} U_{\beta j} U^*_{\alpha j} e^{i\frac{\Delta m_{ij}^2}{2E}L}, \tag{2.10}$$

which shows that neutrino flavor oscillations generally occur for non-zero squared-mass differences $\Delta m_{ij}^2 \equiv m_i^2 - m_j^2$. More specifically, measurements involving accelerator, reactor, solar and atmospheric neutrinos predict two non-zero squared-mass differences [5]

$$\Delta m_{12}^2 = (7.58 \pm 0.18) \cdot 10^{-5}\text{eV}^2, \tag{2.11}$$
$$\Delta m_{32}^2 = (2.453 \pm 0.034) \cdot 10^{-3}\text{eV}^2, \tag{2.12}$$

which in turn require at least two non-zero masses, the third one may or may not be massive. The origin of these masses remains an open question, but it certainly lies beyond the SM.

2.3.2 Baryon asymmetry

The second fundamental puzzle can be stated in simple terms as follows: why is there only matter around us but no antimatter? What is the origin of this baryon

asymmetry? Measurements of the CMB tell us that the baryon number density n_B in the Universe is quite small but a non-zero fraction of the photon number density n_γ, whereas the number density $n_{\bar{B}}$ of anti-baryons is basically zero. Concretely, the baryon asymmetry is given as [5, 48]

$$\frac{n_B - n_{\bar{B}}}{n_\gamma} = \frac{n_B}{n_\gamma} = (6.133 \pm 0.027) \cdot 10^{-10}. \tag{2.13}$$

It is generally assumed that this number was initially zero and that it was produced dynamically in the early Universe, in a process called *baryogenesis*. A.D. Sakharov showed that for a successful baryogenesis, one has to fulfill three conditions [49], namely

- the non-conservation of baryon number,
- the violation of charge (C) and charge-parity (CP) symmetry,
- a departure from thermal equilibrium.

The first condition is obvious if the Universe initially started out with $n_B = 0$. The violation of C and CP symmetry is necessary since any process generating baryon number would have the same rate as its C- or CP-conjugate process, generating anti-baryon number. Hence, no baryon asymmetry would be generated. A system in thermal equilibrium does not allow for a non-zero rate of baryon number creation without the same rate for destruction, so again no baryon asymmetry would be generated. In the SM, the chiral anomaly can lead to baryon number generation via so-called sphaleron processes [50, 51]. Such a process describes the transition between different electroweak vacuum configurations, in which baryon number and lepton number are violated in a way such that their difference is conserved. Then, baryon number can be created from a non-zero lepton number. The origin of the latter again demands an explanation. The only source of CP-violation in the SM is the Cabbibo-Kobayashi-Maskawa matrix, responsible for quark mixing. It was however shown that it provides insufficient amounts of CP-violation for a successful baryogenesis [52,53]. A departure from thermal equilibrium can be found in the early Universe during the electroweak phase transition. It was shown that a strong first order phase transition is required for generating the observed baryon asymmetry [54]. It turned out however, that for the SM Higgs mass $m_H \approx 125\,\text{GeV}$ [3, 4], this transition was a smooth crossover and a first order phase transition would only be possible for a much lower mass, $m_H \lesssim 80$ GeV [55]. Due to these findings, it can be concluded that the SM alone is not able to explain the origin of the baryon asymmetry of the Universe.

Chapter 3

General introduction to sterile neutrinos

This chapter serves as a general introduction to the main actor of this thesis, the sterile neutrino. There is a large variety of phenomenology associated with its existence, depending on the number of sterile flavors, their masses and couplings to other fields.

A sterile neutrino is the right-handed counterpart to the left-handed SM neutrino, which makes it a singlet also under the weak SU(2) gauge symmetry. This is the reason for the term 'sterile', as opposed to the SM neutrino often being referred to as 'active'. It may come in any number of different flavors, even though the most natural number would appear to be three, just like the active neutrino appears in three flavors. As the sterile neutrino is uncharged under all gauge groups of the SM, it is possible to introduce a Majorana mass for it without violating any gauge symmetry. In order to find solutions to SM problems, a connection between the sterile sector and the SM sector is desirable. Coupling active and sterile neutrinos via Yukawa interactions with the Higgs field is in accordance with all SM gauge symmetries. In this setup, we may describe the sterile neutrino with a Majorana spinor N and extend the SM Lagrangian by

$$\mathcal{L} = \frac{1}{2}\sum_i \bar{N}_i \left(i\partial\!\!\!/ - M_i\right) N_i - \sum_{\alpha,i} \left(\bar{N}_i \widetilde{\varphi}^\dagger h_{i\alpha} \ell_\alpha + \text{h.c.}\right). \tag{3.1}$$

Here, the index i counts the number of sterile flavors, $\widetilde{\varphi} = i\sigma^2\varphi^*$ is the conjugate Higgs doublet, $\ell_\alpha = (\nu_{L\alpha}, e_{L\alpha})^\top$ is the left-handed lepton doublet, the Yukawa couplings are denoted by $h_{i\alpha}$ and the Majorana masses by M_i.

With this setup, we may not only find a suitable dark matter candidate but also a possible way out of other problems we discussed in the previous chapter. Solving more than one problem at once is challenging however, as different solutions generally require different sterile neutrino masses.

3.1 Different mass scales solve different problems

3.1.1 Seesaw-mechanism

For the purpose of illustration, we consider the simple case of only one sterile and one active neutrino in (3.1). Generally, we can express the sterile neutrino field N through a right-chiral field ν_R as

$$N = \nu_R + (\nu_R)^c, \tag{3.2}$$

where $(\nu_R)^c$ is the CP-conjugate field of ν_R. In the broken phase of electroweak symmetry, the Higgs field adopts its vacuum expectation value $\langle\widetilde{\varphi}\rangle = (v/\sqrt{2}, 0)^\top$ with $v \simeq 246$ GeV [5]. In that case, we can rewrite the mass terms in (3.1) as

$$\mathcal{L}_m = \frac{1}{2}\begin{pmatrix}\overline{\nu_L} & \overline{(\nu_R)^c}\end{pmatrix}\begin{pmatrix}0 & m_D\\ m_D & M\end{pmatrix}\begin{pmatrix}(\nu_L)^c\\ \nu_R\end{pmatrix} + \text{h.c.}, \tag{3.3}$$

where $m_D \equiv h_\alpha v/\sqrt{2}$ is a Dirac mass. Diagonalizing the mass matrix in the limit $M \gg m_D$, yields the eigenvalues

$$m_1 = -\frac{m_D^2}{M}, \tag{3.4}$$

$$m_2 = M. \tag{3.5}$$

The negative sign of the first eigenvalue can be absorbed via redefinitions of the fields. The corresponding mass eigenfields read

$$\nu_m = \nu_L + (\nu_L)^c - \frac{m_D}{M}\Big(\nu_R + (\nu_R)^c\Big), \tag{3.6}$$

$$N_m = \nu_R + (\nu_R)^c + \frac{m_D}{M}\Big(\nu_L + (\nu_L)^c\Big). \tag{3.7}$$

We see that the introduction of a right-chiral neutrino field and a heavy scale M yields two new mass eigenfields, one of which is very light and almost purely left-handed and the other is much heavier and almost purely right-handed. The heavier one field becomes by choosing larger M, the lighter the other field becomes as a result, hence this is called the seesaw mechanism.

The light field is identified with the SM neutrino. Although the individual SM neutrino masses are unknown, combined results from CMB measurements and baryon acoustic oscillations suggest the upper limit on the sum of all three active neutrino masses [5, 6]

$$\sum m_\nu < 0.12\,\text{eV}. \tag{3.8}$$

Let us for the moment assume a neutrino mass $m_1 \sim 10^{-2}$eV. Then we can give a rough estimate of the scale M that is necessary to produce this mass via the seesaw

mechanism. For Yukawa couplings comparable to the ones for the charged leptons or quarks, i.e., for masses between $m_D \sim m_e$ and $m_D \sim m_t$, this would require a Majorana mass $M \sim 10^4$ GeV up to $M \sim 10^{15}$ GeV respectively. Alternatively, the small SM neutrino masses can simply be the result of much smaller Yukawa couplings and smaller values for M.

3.1.2 Leptogenesis

Regarding the origin of the baryon asymmetry of the Universe, sterile neutrinos may enable a successful baryogenesis via so-called *leptogenesis*, originally proposed in [56]. In this scenario, the first step is the creation of a lepton asymmetry, the second step is converting it into a baryon asymmetry via sphaleron processes. Sterile neutrinos can provide for additional CP violation to the SM through their Yukawa couplings. If the couplings are small enough, the sterile neutrinos may be far from thermal equilibrium and never even reach it. Furthermore, their Majorana mass term violates lepton number conservation. Thus, a lepton asymmetry can be created and subsequently baryogenesis can take place, since the Sakharov conditions can be fulfilled.

There exist various possible realizations of leptogenesis, involving different mass scales. In the original scenario, also called thermal leptogenesis, lepton asymmetry is created via the out-of-equilibrium decay of heavy Majorana neutrinos. One generally requires very high masses, $M \gg$ TeV. Thermal leptogenesis may be resonantly enhanced by nearly mass-degenerate sterile neutrinos, referred to as resonant leptogenesis [57]. This may be realized with lighter masses, $M \sim 1$ TeV. Hence, the same scale necessary to explain SM neutrino masses and mixing, can account for the baryon asymmetry of the Universe with these mechanisms. Leptogenesis can also take place via sterile neutrino oscillations [58], which is possible for even smaller masses, $M \sim \mathcal{O}(\text{GeV})$.

The Majorana mass scales mentioned in this section are way above the mass scale at which the sterile neutrino is a viable dark matter candidate, which is the keV-scale. This scale will be our main focus for the rest of this thesis and we introduce some generalities on sterile neutrino dark matter in the following section.

3.2 Sterile neutrino dark matter today

If sterile neutrinos are supposed to make up the dark matter, they must have been produced in the early Universe at some point and they have to fulfill certain conditions. Generally, the particles should be almost stable, with lifetimes being of the same order as the age of the Universe. Otherwise, they would mostly have decayed already. Furthermore they must be present in the correct abundance, see eq. (1.1).

These conditions give constraints on the sterile neutrino masses and their couplings to the SM neutrinos. Additional constraints from observations can be obtained for concrete production mechanisms, which deserve detailed inspections on their own.

All relevant processes we will consider take place at temperatures far below the electroweak scale, where the Higgs field acquires its vacuum expectation value v. The common way of parameterizing the coupling of the sterile neutrino with mass M to an active neutrino of flavor α is via the active-sterile mixing angle

$$\theta_\alpha \equiv \frac{|h_\alpha|\, v}{\sqrt{2}M}, \tag{3.9}$$

where h_α denotes the Yukawa coupling. We recast the total mixing angle through

$$\sin^2(2\theta) \approx 4 \sum_\alpha \theta_\alpha^2, \tag{3.10}$$

which is the parameter that can be constrained experimentally.

3.2.1 Phase space constraints

The first model-independent parameter constraint on sterile neutrino dark matter comes from the fact that neutrinos are fermions and thus underly the Pauli exclusion principle. Consider for example a galaxy with a fixed portion of its mass coming from sterile neutrinos that are contained in it. To keep it simple, we assume that there is only one flavor of sterile neutrinos. By decreasing the sterile neutrino's mass M, one increases the particle number. Pauli blocking requires that the phase space density does not exceed the density of a degenerate Fermi gas, leading to a lower bound on M. By studying some of the most compact dwarf spheroidal galaxies (see, e.g., [59]), ref. [60] finds the lower limit

$$M \geq 0.13\,\mathrm{keV} \tag{3.11}$$

The strength of this bound can be improved if the phase space density is specified, which is however model-dependent as the density is determined by the production mechanism. When the production of sterile neutrinos terminates at some early point in time, the shape of their spectrum is fixed and will only be subject to redshift. At later times, structure formation sets in and the particles start clustering differently in galaxies, galaxy clusters, voids and so forth. Then the coarse-grained density $\tilde{f}$, i.e., the distribution averaged over macroscopic parts of space, becomes inhomogeneous. Naturally, it grows in underdense regions and gets diluted in overdense regions. Since sterile neutrino dark matter is basically collisionless, Liouville's theorem guarantees that its maximum $f_{\max}$ never exceeds the maximum of the initial primordial distribution,

$$\tilde{f}_{\max}(t) \leq f_{\max}. \tag{3.12}$$

A mass bound derived from this inequality is also referred to as a Tremaine-Gunn bound [61]. The left-hand side of this inequality can be determined with help of observations, only the right-hand side is a prediction of a particular production mechanism. In their original work, Tremaine and Gunn assumed that the central regions of bound systems formed by neutrinos resemble isothermal spheres with a core radius r_c and a 1D velocity dispersion σ, with a maximum coarse-grained density

$$\tilde{f}_{\max} = \frac{9\sigma^2}{M^4 4\pi G (2\pi\sigma^2)^{3/2} r_c^2}. \tag{3.13}$$

The particles are assumed to follow a Fermi-Dirac distribution initially, with the maximum

$$f_{\max} = \frac{2g}{(2\pi\hbar)^3}, \tag{3.14}$$

where g is the number of allowed helicity states. Then (3.12) leads to the lower mass bound

$$M^4 \geq \frac{9(2\pi)^{1/2}\hbar^3}{4gG\sigma r_c^2}. \tag{3.15}$$

Newer studies rely on more recent observations of, e.g., dwarf spheroidal galaxies and more involved coarse-graining techniques to estimate the left-hand side of (3.12) and obtain a lower mass bound in this fashion. For non-resonantly produced sterile neutrino dark matter, [60] finds the lower bound

$$M \gtrsim 1.74\text{keV}, \tag{3.16}$$

where the initial primordial distribution has been calculated using the publicly available codes from [62] and [63]. Both codes produce similar distributions in that scenario and agree with our results in chapters 5 and 6. For resonantly produced sterile neutrino dark matter, [64] gives

$$M \gtrsim 1\text{keV}, \tag{3.17}$$

which well agrees with [60] and is also the limit we adopted in [1]. We will display this limit in chapter 6.

3.2.2 X-ray constraints

The second very general constraint is based on active-sterile mixing via the Yukawa couplings in (3.1). Due to these couplings, the sterile neutrino naturally is subject to decay, with one possible decay channel involving a photon in the final state. Even though this is not the primary decay channel, the final state photon potentially leads to a detectable signal, which would fix M as well as $\sin^2(2\theta)$. The primary decay

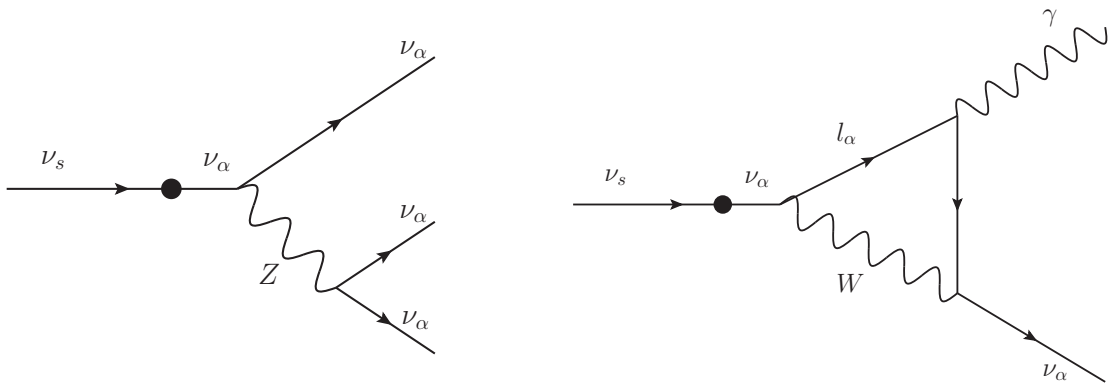

Figure 3.1: Left: Tree-level decay of a sterile neutrino into three active neutrinos. The big blob represents the active-sterile mixing. Right: One-loop decay of a sterile neutrino into an active neutrino and a photon.

channel is a tree-level decay into three active neutrinos, mediated by a Z-boson. The corresponding decay rate reads [65]

$$\Gamma_{3\nu} = \frac{G_F^2}{768\pi^3} M^5 \sin^2(2\theta), \tag{3.18}$$

where $G_F = 1.1663787(6) \cdot 10^{-5}\,\mathrm{GeV}^{-2}$ [5] is the Fermi coupling constant. The rate of the secondary decay into an active neutrino and a photon reads [66]

$$\Gamma_{\nu\gamma} = \frac{9\alpha_{\mathrm{EM}} G_F^2}{1024\pi^4} M^5 \sin^2(2\theta), \tag{3.19}$$

with the fine-structure constant $\alpha_{\mathrm{EM}} = 7.2973525693(11) \cdot 10^{-3} \approx 1/137$ [5]. Both decays are depicted in figure 3.1. For typical values $\sin^2(2\theta) \lesssim 10^{-7}$ for the active-sterile mixing angle, which we will encounter in chapter 5, both channels can still yield a sterile neutrino lifetime that can well be above the age of the Universe. In the neutrino plus photon decay, both product particles carry away half of the energy of the comparably massive sterile neutrino. For keV-masses, the photon energy will be located in the X-ray spectrum. A detectable signal can originate from regions where a sizable amount of dark matter accumulates and it is actively searched for in various places, like galaxies, galaxy clusters and the diffuse X-ray background. The latter is due to lots of obscured and unobscured active galactic nuclei. It is a rather featureless astrophysical background, against which other decay line may be searched for. If a line in the X-ray spectrum is measured, its position would fix the sterile neutrino mass and its intensity would then fix the mixing angle via (3.19). If we assume that the dark matter abundance is solely due to sterile neutrinos and no line feature of an expected decay is found, the corresponding combination of mass and mixing angle is excluded. There is a number of measurements from

different observatories that have already explored large regions in the $(M, \sin^2(2\theta))$-plane. For masses $\lesssim 10$ keV, strong limits come from X-ray telescopes like Chandra and XMM-Newton [67, 68]. The intermediate mass range ($10\text{keV} \lesssim M \lesssim 50\text{keV}$) is strongly constrained by NuSTAR observations [69], higher masses are covered, e.g., by INTEGRAL [70]. Over the years, new telescopes with increasingly high resolutions have been able to probe smaller and smaller mixing angles and thus limiting the available parameter space more and more. We show current, combined constraints in chapter 6.

A few years ago, the detection of an unidentified line at energy $E \simeq 3.55$ keV was first reported in spectra of galaxy clusters and the Andromeda galaxy [71, 72]. Since then, it was reported in several more clusters, as well as in the galactic center of the Milky Way [73]. It can be interpreted as the radiative decay of a sterile neutrino with a mass $M = 7.1$ keV, the measured intensity would correspond to a mixing angle $\sin^2(2\theta) \simeq (2 - 20) \cdot 10^{-11}$ according to [72]. The true origin of this line is however not yet clear. Uncertainties from astrophysical background as well as systematic errors in instrumental calibration make a definite identification very difficult, see, e.g., [74] for a review.

3.3 Production in the early Universe

Assuming that no sterile neutrinos existed early on from the very beginning of the Universe, one needs a production mechanism in order to explain the relic dark matter abundance. We will only deal with scenarios in which the production purely relies on non-zero active-sterile mixing angles. Besides this mechanism, which is by far the most studied one in the literature, there exist mechanisms for sterile neutrino production that do not rely on active-sterile mixing or only partly. Popular ones include the decay of a heavy scalar field into sterile neutrinos [75] or thermal overproduction with subsequent entropy dilution [76].

3.3.1 Thermal production via mixing

Sterile neutrinos that mix with the SM neutrinos are a suitable dark matter candidate. The combined constraints from phase space considerations and X-ray observations suggest a viable particle mass in the keV range, which would make them a warm dark matter candidate. For non-vanishing active-sterile mixing angles, sterile neutrinos can be produced thermally through oscillations and scatterings in the early Universe. Assuming that they have no initial abundance, this would inevitably lead to a build-up of a sterile neutrino reservoir, but thermal equilibrium would never be reached for sufficiently small mixing angles. This minimal scenario of thermal sterile neutrino production in the context of dark matter was proposed by Dodelson

and Widrow [11], thus it is often referred to as Dodelson-Widrow (DW) scenario. In this scenario, sterile neutrinos are produced at high temperatures, where active neutrinos are in thermal equilibrium with the other SM particles. Active-sterile oscillations are influenced by interactions of active neutrinos with the rest of the SM plasma. On the one hand, the active-neutrino scattering rate can drive scattering-induced decoherence and states that are purely active initially, may collapse into sterile states. On the other hand, through coherent forward scatterings off of particles in the plasma, active neutrinos acquire thermal masses which may suppress the in-medium mixing with sterile neutrinos (cf. section 4.3). Assuming temperatures far below the electroweak scale, $T \ll 100$ GeV, these considerations generally lead to sterile neutrino production rates that are maximal around $T \sim \mathcal{O}(100\,\mathrm{MeV})$ for sterile neutrinos masses $M \sim \mathcal{O}(\mathrm{keV})$ [11, 16–19].

3.3.2 Mass bounds from structure formation

Sterile neutrinos produced in the Dodelson-Widrow scenario are subject to an additional, important lower mass bound from structure formation, which however depends on the shape of their distribution function. Structure formation, including, e.g., the formation of galaxies and galaxy clusters, is influenced by the free-streaming length of the dark matter particles. On scales above the free-streaming length, warm dark matter acts quite similar to cold dark matter. There it does not disturb the clustering of ordinary matter to a great extent. On smaller scales however, it can suppress structure formation as it tends to wash out the seeds of gravitational collapse.

Simulations of structure formation in the presence of warm dark matter require the linear warm dark matter power spectrum as input [14], which can be obtained from the distribution function. The outcome of such simulations can then be compared to observations which probe the power spectrum, which in turn constrains the free-streaming length and thus the viability of the warm dark matter scenario under consideration. A widely used probe is the Lyman-α forest, a series of absorption lines in spectra of distant objects (like quasars) due to neutral hydrogen in the intergalactic medium. The hydrogen atoms absorb UV photons from the source, raising their bound electron from the ground state to the first excited state. This process is called the Lyman-α transition. Hydrogen clouds at different redshifts produce absorption lines that we observe at different wavelengths, thus we generally see not only one line but multiple lines, i.e., a forest. The Lyman-α forest is a widely used tool for probing density fluctuations at intergalactic scales. A similar probe used to study the onset of structure formation is the 21-cm line [77], a hydrogen emission line due to the transition of the electron between the hyperfine levels of the ground state, also called the spin-flip transition.

Structure formation simulations generally assume that the dark matter is a thermal relic, meaning that it decoupled from the primordial plasma very early on and follows a thermal distribution. Then one can simply relate the free-streaming length to the particle mass and translate upper bounds on the former to lower bounds on the latter [78]. Due to symmetry arguments in the evolution equations of linear perturbations, thermal relics produce the same cutoff in the linear matter power spectrum as sterile neutrinos produced in the DW scenario [79]. Thus, warm dark matter simulations with thermal relics can also be used to derive bounds on sterile neutrinos.

A direct relation between the mass m_x of a thermal relic and the mass M of a sterile neutrino can be derived as follows. Just like the thermal relic, active neutrinos are in thermal equilibrium at high temperatures and they have the distribution

$$f_\nu = \frac{1}{e^{p/T_\nu} + 1}. \tag{3.20}$$

By integrating over momenta, one obtains the relation [80, 81]

$$\Omega_\nu h^2 = \frac{m_\nu}{93\text{eV}} \tag{3.21}$$

between the relic density and total mass of the neutrinos. The thermal relic has the same distribution, but with a temperature T_x that is much lower than T_ν since it decoupled much earlier. Then its relic density is given by

$$\Omega_x h^2 = \left(\frac{T_x}{T_\nu}\right)^3 \frac{m_x}{93\text{eV}}. \tag{3.22}$$

Now consider sterile neutrino warm dark matter from the DW scenario. It is supposedly approximated by a suppressed version of the distribution of active neutrinos [18, 82],

$$f_{\text{sterile}} \approx \chi f_{\text{active}} = \frac{\chi}{e^{p/T_\nu} + 1}, \tag{3.23}$$

with the suppression factor $\chi \in [0, 1]$ being a function of the active-sterile mixing angle. In this case, the relic density reads

$$\Omega_{\text{DM}} h^2 = \chi \frac{M}{93\text{eV}}. \tag{3.24}$$

Both, the thermal relic scenario and the DW scenario, impact structure formation equally, assuming equal relic densities and mean velocities. Requiring equal mean velocities yields

$$\frac{\langle p_s \rangle \, T_\nu}{M} = \frac{3.15 T_x}{m_x}, \tag{3.25}$$

which gives a direct relation between the masses of both scenarios. Here, $\langle p_s \rangle$ is the mean momentum of the sterile neutrino spectrum in units of T_ν, the thermal

distribution has a mean momentum $\langle p_x \rangle \approx 3.15 T_x$. Assuming that both scenarios yield the relic dark matter density, we find

$$M = \frac{\langle p_s \rangle}{3.15} m_x^{4/3} \left(\Omega_{\rm DM} h^2 \, 93 \, {\rm eV} \right)^{-1/3}, \tag{3.26}$$

where we used (3.22) to express T_x via m_x. The key assumption behind this relation is that the sterile neutrino spectra in the DW scenario can be described by (3.23). We explicitly compute them in chapter 5 and refer to figure 5.1, where we show them together with a thermal spectrum for comparison. We find relatively similar spectra for low masses, $M \sim 1$ keV. Their difference does not exceed 20%, which has negligible impact on the mass bounds [60, 64] and justifies the approximation a posteriori. Strong bounds on the mass of a thermal relic based on Lyman-α observations come from [83] and [79], both reporting $m_x > 5.3$ keV (95% confidence level), which translates to

$$M > 34 \, {\rm keV}. \tag{3.27}$$

Besides the Lyman-α forest, observations of the 21-cm line have been used to constrain the mass of Dodelson-Widrow sterile neutrinos in a recent study [77]. Their analysis predicts that in order to be compatible with observations, the sterile neutrino mass should be

$$M = 63^{+19}_{-35} {\rm keV}, \tag{3.28}$$

which also provides an upper limit for the first time. The lower limits from these different studies are compatible with each other and they reach far into the region that has already been excluded by X-ray observations. These predictions exclude the Dodelson-Widrow scenario as a viable dark matter scenario.

3.3.3 Resonant production

One possible way to circumvent the strong constraints in the DW scenario is the introduction of a large primordial lepton asymmetry. This dark matter scenario was introduced by Shi and Fuller [15]. If large enough, such an asymmetry can shift the thermal masses of active neutrinos up to the level of sterile neutrino masses in the keV-range, which is not possible with only SM interactions and lepton asymmetries as low as the baryon asymmetry. Potential mass level crossings result in Mikheyev-Smirnov-Wolfenstein (MSW) resonances [84, 85], at which the in-medium active-sterile mixing angle peaks. Then very efficient conversion of active to sterile neutrinos takes place, which simultaneously depletes the lepton asymmetry. It is a trade-off in which a surplus of neutrinos over anti-neutrinos (or vice-versa) will be transformed into an abundance of sterile neutrinos with negative (positive) helicity, thus the net lepton number decreases. Resonant enhancements make sterile

neutrino production much more efficient than purely thermal production, requiring smaller mixing angles and thus potentially escaping the upper limits from X-ray constraints. Furthermore, resonant production generally results in a non-thermal spectrum, which can be colder than in the DW scenario. Then no simple relation like (3.26) exists and one can potentially evade Lyman-α constraints.

The lepton asymmetries, needed to produce the complete dark matter abundance without running into X-ray or Lyman-α constraints, are generally quite large compared to the baryon asymmetry. Typically, the total lepton asymmetry n_L is given as the number density of leptons minus the number density of anti-leptons, either in units of the photon number density n_γ or the entropy density s. The Shi-Fuller scenario typically requires values $n_L/s \gtrsim 10^{-6}$ in order to be a viable dark matter scenario, which we will use in section 5.2.

3.3.4 Upper bounds on lepton asymmetry

Large primordial lepton asymmetries can impact the evolution of the early Universe and have measurable effects on big bang nucleosynthesis (BBN) and the CMB. Upper limits on the lepton asymmetry can be derived from measurements of light element abundances, which form during BBN. The latter is a stage in the cosmological evolution in which protons and neutrons start to form nuclei. The temperature of the cosmic plasma has dropped to $T \sim 0.1$ MeV at this point, which so far corresponds to the highest temperature, i.e., the earliest epoch that can be directly probed by measurements [86].

We know that the Universe is electrically neutral, which implies that large lepton asymmetries lie mostly in the neutrinos, while the charged sector has a negligible asymmetry of the order of the baryon asymmetry or below. Neutrino asymmetries are often expressed in terms of the neutrino degeneracy parameters $\xi_{\nu_\alpha} = \mu_{\nu_\alpha}/T$, where μ_{ν_α} are the chemical potentials, as [87]

$$\eta_{\nu_\alpha} \equiv \frac{n_{\nu_\alpha} - n_{\bar{\nu}_\alpha}}{n_\gamma} \approx \frac{1}{12\zeta(3)} \left(\frac{T_{\nu_\alpha}}{T_\gamma}\right)^3 (\pi^2 \xi_{\nu_\alpha} + \xi_{\nu_\alpha}^3). \tag{3.29}$$

The total asymmetry is obtained by summing over all flavors,

$$\eta_\nu = \sum_\alpha \eta_{\nu_\alpha}. \tag{3.30}$$

Non-zero chemical potentials have two effects on BBN. First of all, they modify the

overall energy density ρ_ν in the neutrino sector according to

$$\rho_\nu = \sum_\alpha \int \frac{d^3k}{(2\pi)^3} k \Big(f_{\rm F}(k-\mu_\alpha) + f_{\rm F}(k+\mu_\alpha) \Big) \tag{3.31}$$

$$= \frac{7\pi^2}{120} \sum_\alpha T_{\nu_\alpha}^4 \left[1 + \frac{30}{7} \left(\frac{\xi_\alpha}{\pi} \right)^2 + \frac{15}{7} \left(\frac{\xi_\alpha}{\pi} \right)^4 \right], \tag{3.32}$$

where $f_{\rm F}(x) = 1/(e^{x/T_{\nu_\alpha}} + 1)$ is the Fermi-Dirac distribution and T_{ν_α} denotes the neutrino temperature. This increase is often expressed in terms of an excess of the effective number of neutrinos, $\Delta N_{\rm eff}$, with [88]

$$\Delta N_{\rm eff} = \frac{15}{7} \sum_\alpha \left[2 \left(\frac{\xi_\alpha}{\pi} \right)^2 + \left(\frac{\xi_\alpha}{\pi} \right)^4 \right]. \tag{3.33}$$

Non-zero chemical potentials always lead to a non-negative $\Delta N_{\rm eff}$ and thus and increased energy density. This leads to a higher expansion rate of the Universe, implying an earlier freeze-out of weak interaction processes. Ultimately, the neutron-to-proton ratio decreases as a result. Secondly, a positive chemical potential in the electron flavor decreases the neutron-to-proton ratio according to the beta decay and inverse decay equilibrium processes $p + e \leftrightarrow n + \nu_e$. Both effects naturally alter the measured light element abundances, like the helium-4 abundance.

Simulations of BBN at $T \lesssim 1$ MeV can predict the light element abundances and give limits on what values the neutrino asymmetries can take. A recent analysis [89] found that, using two different codes for their simulations, the neutrino degeneracy parameters either take the value $\xi_{\nu_\alpha} = 0.001 \pm 0.016$ or $\xi_{\nu_\alpha} = 0.021 \pm 0.016$. Not only are there sizable, statistical uncertainties, the systematic uncertainties due to the different codes are also very large. The upper limits on ξ_{ν_α} imply the upper limits $\eta_\nu < 0.013$ and $\eta_\nu < 0.028$ respectively.

We can translate asymmetries, which are normalized to the photon number densities, to ones which are normalized to the entropy density, using (see, e.g., [90])

$$n_\gamma = \frac{2\zeta(3)}{\pi^2} T^3 \tag{3.34}$$

and

$$s = \frac{2\pi^2}{45} g_* T^3. \tag{3.35}$$

Here, g_* counts the relativistic degrees of freedom and is a function of temperature and chemical potentials. For bounds on the lepton asymmetry from BBN, we are interested in temperatures $T \lesssim 1$ MeV. Hence, we use the value of $g_* \approx 3.9$ after electron-positron annihilation [91], which takes place at $T \sim 0.5$ MeV.

We find that the upper limits $\eta_\nu < 0.013$, $\eta_\nu < 0.028$ translate to $n_L/s < 0.0018$ and $n_L/s < 0.0039$ respectively. Ref. [87] finds $\xi = 0.0245 \pm 0.0092\,(1\sigma)$, based on the value of the primordial helium abundance $Y_p = 0.2421 \pm 0.0021$ [92], as well as the baryon asymmetry. Plugging this into (3.29) and converting it into a fraction of the entropy density, one obtains the upper bound

$$\left.\frac{n_L}{s}\right|_{\mathrm{BBN}} \leq 2.5 \cdot 10^{-3} \tag{3.36}$$

on the total lepton asymmetry. This lies within the region of values from [89]. It is used as the upper limit for calculating sterile neutrino abundances in [13] and we also used it in [1].

The large uncertainties in BBN calculations motivate the consideration of additional, more robust limits that take into account CMB measurements. One notable effect of large lepton asymmetries on the CMB, conducted through a non-zero ΔN_{eff}, is a delay of the matter-radiation equality time. This leads to an enhancement of the first acoustic peak in the CMB power spectrum and also influences the position of the following peaks, which is the early integrated Sachs-Wolfe effect [93].

Strong constraints are given in [88], reporting $-0.085 \leq \eta_\nu \leq 0.084$. These numbers are deduced from an analysis of CMB data, which are consistent with BBN but do not rely on direct measurements of the light element abundances. The resulting upper limit on the lepton asymmetry reads

$$\left.\frac{n_L}{s}\right|_{\mathrm{CMB/BBN}} < 0.012. \tag{3.37}$$

More precisely, the absolute value of the lepton asymmetry is constrained and the latter could also be negative. We will update the available parameter space for resonantly produced sterile neutrino dark matter in chapter 6 using this limit.

3.3.5 Uncertainties from QCD

Sterile neutrinos with keV-masses are produced mainly during the QCD epoch of the early Universe. In this epoch, the strongly interacting SM sector undergoes a transition from a quark-gluon plasma into a more dilute hadron gas, which greatly decreases the number of relativistic degrees of freedom g_* (cf. (3.35)) from roughly 60 down to roughly 20 [94]. This already illustrates that hadronic effects are sizable and potentially dominate the plasma behavior. As was shown by numerical simulations on a lattice, the transition is a smooth crossover from one phase to the other, in case of vanishing baryon-chemical potential [20, 21]. This is an accurate assumption for the state of the early Universe at $T \lesssim 130$ GeV, since at this point, the baryon asymmetry (generated at much higher temperatures) is fixed [95] and only a tiny

fraction of the photon density, see (2.13). As reported by the HotQCD collaboration, this smooth but rapid crossover takes place around the temperature [96]

$$T_{\mathrm{QCD}} = (156.5 \pm 1.5)\,\mathrm{MeV}. \tag{3.38}$$

In this regime, one cannot rely on a weakly interacting quark-gluon plasma or a dilute hadron gas as an accurate description of QCD matter. Perturbation theory does not apply and one has to resort to non-perturbative calculations of QCD effects.

In principle, the QCD crossover can have important effects on sterile neutrino production in two ways. On the one hand, the number of relativistic degrees of freedom influences the cosmological expansion through the pressure-energy relation (equation of state) of the matter in the Universe. The expansion directly enters the sterile neutrino production rate. Lattice QCD results have been incorporated into an equation of state [94], which was for the first time used to compute sterile neutrino production in [97]. On the other hand, quarks participate in weak interactions and thus, they naturally enter sterile neutrino reaction rates through interactions of active neutrinos with hadronic degrees of freedom. These interactions contribute to both the real and the imaginary part of the active-neutrino self-energy. Real-part contributions are determined by susceptibilities of the QCD plasma's conserved charges, see section 4.3. Lattice determinations of susceptibilities [98, 99] were included into sterile neutrino evolution equations in [62]. The most difficult to compute are hadronic contributions to the imaginary part of the active-neutrino self-energy, or *opacity*, which can be written as a momentum integral over mesonic spectral functions [100]. Determining these spectral functions on the lattice is challenging. Previous works on resonant sterile neutrino production [62,63] have treated the opacity in different approximations, but it still remains an open question how important the non-perturbative contributions are.

Chapter 4

Non-equilibrium evolution equations

4.1 Notation and setup

We consider the Standard Model augmented by one family of sterile Majorana neutrinos N with Majorana mass M and non-zero Yukawa couplings h_α to all active-neutrino flavors,

$$\mathcal{L} = \mathcal{L}_{SM} + \frac{1}{2}\bar{N}(i\partial\!\!\!/ - M)N - \sum_\alpha \left(\bar{N}\widetilde{\varphi}^\dagger h_\alpha \ell_\alpha + \text{h.c.}\right) \tag{4.1}$$

The sterile neutrino field in the interaction picture reads

$$N(x) = \sum_{\mathbf{k},\lambda} \frac{1}{\sqrt{2k^0 V}} \left[e^{-ik\cdot x} u_{\mathbf{k}\lambda} a_{\mathbf{k}\lambda} + e^{ik\cdot x} v_{\mathbf{k}\lambda} a^\dagger_{\mathbf{k}\lambda}\right], \tag{4.2}$$

with the energy $k^0 = (\mathbf{k}^2 + M^2)^{1/2}$. The spinors u and v satisfy the Majorana condition $u = v^c$, where c denotes charge conjugation. Furthermore, the creation-/annihilation operators fulfill $\{a_{\mathbf{k}\lambda}, a^\dagger_{\mathbf{q}\lambda'}\} = \delta_{\mathbf{k},\mathbf{q}}\delta_{\lambda\lambda'}$ with helicities $\lambda = \pm 1/2$. V denotes the volume of our system. With these operators we define the sterile neutrino phase space density operators as

$$f_{\mathbf{k}\lambda} \equiv a^\dagger_{\mathbf{k}\lambda} a_{\mathbf{k}\lambda}. \tag{4.3}$$

The number operator for left-handed leptons of flavor α reads

$$L_\alpha = \int d^3x \; \ell^\dagger_\alpha \ell_\alpha. \tag{4.4}$$

We will be considering their time evolution at temperatures of a few GeV, where sphaleron processes have long terminated. Then baryon number B is conserved, and its tiny value can be well approximated by zero for our purposes. Furthermore,+ electric charge Q is conserved and exactly zero.

4.2 Equations of motion

The expectation values of the operators introduced above are conserved by Standard Model interactions and thus evolve much more slowly than the other degrees of freedom. Their deviations from equilibrium characterize the non-equilibrium state, and are assumed to be small. We introduce chemical potentials μ_{L_α}, μ_B and μ_Q and denote them collectively by μ in the following. In the infinite volume limit the phase space densities and the lepton number densities $n_{L_\alpha} \equiv L_\alpha/V$ satisfy the evolution equations [101, 102]

$$\dot{f}_{\mathbf{k}\lambda} = -\frac{1}{2k^0}\sum_\alpha \Big\{ \bar{u}_{\mathbf{k}\lambda}\rho_\alpha(k,\mu)u_{\mathbf{k}\lambda}\big[f_{\mathbf{k}\lambda} - f_{\mathrm{F}}(k^0-\mu_{L_\alpha})\big] + \bar{v}_{\mathbf{k}\lambda}\rho_\alpha(-k,\mu)v_{\mathbf{k}\lambda}\big[f_{\mathbf{k}\lambda} - f_{\mathrm{F}}(k^0+\mu_{L_\alpha})\big]\Big\}, \tag{4.5}$$

and

$$\dot{n}_{L_\alpha} = \sum_\lambda \int \frac{d^3k}{(2\pi)^3 2k^0}\Big\{ \bar{u}_{\mathbf{k}\lambda}\rho_\alpha(k,\mu)u_{\mathbf{k}\lambda}\big[f_{\mathbf{k}\lambda} - f_{\mathrm{F}}(k^0-\mu_{L_\alpha})\big] - \bar{v}_{\mathbf{k}\lambda}\rho_\alpha(-k,\mu)v_{\mathbf{k}\lambda}\big[f_{\mathbf{k}\lambda} - f_{\mathrm{F}}(k^0+\mu_{L_\alpha})\big]\Big\}, \tag{4.6}$$

with the spinors u and v which appear in (4.2). Furthermore,

$$\rho_\alpha(k,\mu) \equiv \frac{1}{i}\left[\Delta^{\mathrm{ret}}_\alpha(k,\mu) - \Delta^{\mathrm{adv}}_\alpha(k,\mu)\right] \tag{4.7}$$

is the spectral function which is determined by the retarded and advanced 2-point function

$$\Delta^{\mathrm{ret,adv}}_\alpha(k) = \pm i\int d^4x\,\Theta(\pm t)e^{ikx}\Big\langle\Big\{J_\alpha(x),\bar{J}_\alpha(0)\Big\}\Big\rangle \tag{4.8}$$

of the operator $J_\alpha \equiv \widetilde{\varphi}^\dagger h_\alpha \ell_\alpha$, which couples to $\bar{N}$ in (4.1).

Oftentimes the kinetic equations are expanded in μ. However, for a proper treatment of resonances, which show up in the spectral functions ρ_α, one has to include all orders in μ, which will become more apparent below. The relation of the chemical potentials to the charge densities, to be discussed in the next section, can still be assumed to be linear.

In the broken phase of electroweak symmetry, the 2-point function (4.8) is proportional to the active-neutrino propagator,

$$\Delta_\alpha(k,\mu) = \theta_\alpha^2 M^2 P_{\mathrm{L}}\frac{-1}{\not{k} - \Sigma_\alpha(k,\mu)}P_{\mathrm{R}}. \tag{4.9}$$

Here we have factored the chiral projectors $P_{\mathrm{R,L}} = \frac{1}{2}(1\pm\gamma_5)$ out of the propagator and expressed the couplings through the active-sterile mixing angle (3.9). The active-neutrino self-energy in the plasma rest frame can be approximated as [63, 103]

$$\Sigma^{\mathrm{ret}}_\alpha(\pm k,\mu) = \gamma^0\left(\mp b_\alpha + c_\alpha - \frac{i\Gamma_\alpha}{2}\right), \tag{4.10}$$

with real b_α, c_α. Γ_α is the imaginary part of the refractive index for the active neutrinos [104], and is also referred to as neutrino opacity. $\Gamma_\alpha/2$ is the neutrino damping rate (see e.g. [105]). The function c_α is odd in μ. For the chemical potentials under consideration we only need to keep the linear order in μ for c_α, and we can neglect the μ-dependence of b_α and Γ_α. The advanced self-energy is obtained from (4.10) by replacing $i\Gamma_\alpha \to -i\Gamma_\alpha$. Then one obtains the spectral function

$$\rho_\alpha(\pm k, \mu) = \frac{\theta_\alpha^2 \Gamma_\alpha M^2}{[M^2 + 2k^0(b_\alpha \mp c_\alpha)]^2 + (k^0\Gamma_\alpha)^2} P_{\mathrm{L}}(2k^0 \not{k} - M^2\gamma^0)P_{\mathrm{R}}. \tag{4.11}$$

A quick calculation yields

$$\bar{u}_{\mathbf{k}\pm}\rho_\alpha(k,\mu)u_{\mathbf{k}\pm} = \frac{\theta_\alpha^2 \Gamma_\alpha M^4 (k^0 \mp |\mathbf{k}|)}{[M^2 + 2k^0(b_\alpha - c_\alpha)]^2 + (k^0\Gamma_\alpha)^2}, \tag{4.12}$$

$$\bar{v}_{\mathbf{k}\pm}\rho_\alpha(-k,\mu)v_{\mathbf{k}\pm} = \frac{\theta_\alpha^2 \Gamma_\alpha M^4 (k^0 \pm |\mathbf{k}|)}{[M^2 + 2k^0(b_\alpha + c_\alpha)]^2 + (k^0\Gamma_\alpha)^2}. \tag{4.13}$$

Resonances occur when a square bracket in the denominator of (4.12) or (4.13) vanishes. This can happen when c_α is large enough and has the appropriate sign. For a given sign of an initial lepton asymmetry, only one of the expressions (4.12) and (4.13) can lead to resonances. Moreover, at leading order in $M/|\mathbf{k}|$ only the terms containing $\bar{u}_{\mathbf{k}-}\rho_\alpha u_{\mathbf{k}-}$ or $\bar{v}_{\mathbf{k}+}\rho_\alpha v_{\mathbf{k}+}$ will contribute in the evolution equations. The subleading terms will be dropped in the following.

Due to the isotropy of the universe the phase space density only depends on $|\mathbf{k}|$. Then the Hubble expansion is taken into account by replacing

$$\dot{f}_{\mathbf{k}\lambda} \to \Big(\partial_t - H|\mathbf{k}|\partial_{|\mathbf{k}|}\Big) f_{\mathbf{k}\lambda}. \tag{4.14}$$

The Hubble parameter is given by

$$H = \sqrt{\frac{8\pi\rho}{3M_{\mathrm{Pl}}^2}}, \tag{4.15}$$

where ρ is the energy density and $M_{\mathrm{Pl}} \simeq 1.22 \cdot 10^{19}$ GeV is the Planck mass. By using $K \equiv |\mathbf{k}|a(t)/a(t_{\mathrm{end}})$ as an independent variable, where a is the scale factor, (4.14) turns into $\partial_t f_{K\lambda}$ and the equation for f becomes an ordinary differential equation. $a(t_{\mathrm{end}})$ is the scale factor at the time corresponding to the temperature $T_{\mathrm{end}} = 10$ MeV at which we compute the final abundances in the next chapter. For lepton number densities, the Hubble expansion is taken into account through the replacement

$$\dot{n}_{L_\alpha} \to \Big(\partial_t + 3H\Big) n_{L_\alpha}. \tag{4.16}$$

The term proportional to H is eliminated by considering the differential equation for n_{L_α}/s where s is the entropy density. Finally, the time derivatives are replaced by temperature derivatives via the time-temperature relation [106]

$$\frac{dT}{dt} = -TH(T)3c_s^2(T), \tag{4.17}$$

with the speed of sound c_s. Once the solutions to (4.5) are obtained, we obtain the total energy density at the final temperature T_{end} as

$$\rho_s(T_{\text{end}}) = \sum_\lambda \int \frac{d^3k}{(2\pi)^3} \sqrt{\mathbf{k}^2 + M^2} f_{\mathbf{k}\lambda}(T_{\text{end}}). \tag{4.18}$$

If we know the energy density today at temperature T_0, we use $\rho_s = \Omega_s \rho_c$ and obtain the fraction of the present dark matter abundance via

$$\frac{\Omega_s}{\Omega_{\text{DM}}} = \frac{1}{\Omega_{\text{DM}} h^2 \frac{\rho_c}{h^2 s(T_0)}} \frac{\rho_s(T_0)}{s(T_0)}, \tag{4.19}$$

with $\Omega_{\text{DM}} h^2 \approx 0.12$ and $\rho_c/h^2 s(T_0) \approx 3.64$ eV [6]. Since the ratio ρ_s/s is conserved in a comoving volume element of the Universe at temperatures $T \leq T_{\text{end}}$, we can replace T_0 by T_{end} in the rightmost fraction. This yields the final expression

$$\frac{\Omega_s}{\Omega_{\text{DM}}} \approx \frac{1}{0.437\text{eV}\, s(T_{\text{end}})} \sum_\lambda \int \frac{d^3k}{(2\pi)^3} \sqrt{\mathbf{k}^2 + M^2} f_{\mathbf{k}\lambda}(T_{\text{end}}). \tag{4.20}$$

4.3 Active-neutrino self-energy

4.3.1 Real parts

Interactions of active neutrinos with the ambient heat bath contribute to their self-energy. Its real part stems from the one-loop diagrams in figure 4.1. For vanishing chemical potentials, the real part b_α arises at $\mathcal{O}\big(G_F/m_W^2\big)$, where G_F is the Fermi constant and m_W is the W-boson mass. It reads [97, 104]

$$b_\alpha = \frac{8\sqrt{2} G_F}{m_W^2} k^0 \left[\cos^2\theta_{\text{W}} \frac{7\pi^2 T^4}{360} + \int \frac{d^3p}{(2\pi)^3} \frac{f_{\text{F}}(E_\alpha)}{E_\alpha} \left(\frac{4}{3}\mathbf{p}^2 + m_\alpha^2 \right) \right], \tag{4.21}$$

where θ_{W} is the weak mixing angle, $E_\alpha \equiv (\mathbf{p}^2 + m_\alpha^2)^{1/2}$, and m_α is the mass of the charged lepton of flavor α. We have neglected the masses of active neutrinos. b_α is positive, which corresponds to an index of refraction greater than 1, or a negative thermal mass squared. The leading contribution due to non-zero chemical potentials

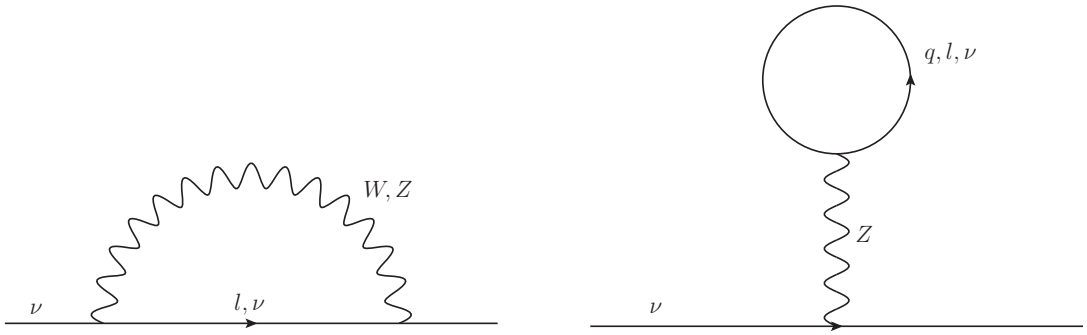

Figure 4.1: Leading contributions to the real part of the active-neutrino self-energy. Left: bubble diagram, contributing to (4.21). Right: tadpole diagram, contributing to (4.22).

can have either sign. It arises at $\mathcal{O}\big(G_F\big)$ [62, 63, 104],

$$c_\alpha = \sqrt{2}G_F\bigg[2n_{\nu_\alpha} + \sum_{\beta\neq\alpha} n_{\nu_\beta} + \left(\frac{1}{2} + 2\sin^2\theta_{\rm W}\right)n_{e_\alpha} - \left(\frac{1}{2} - 2\sin^2\theta_{\rm W}\right)\sum_{\beta\neq\alpha} n_{e_\beta} - \frac{1}{2}n_B + \left(1 - 2\sin^2\theta_{\rm W}\right)n_Q^{\rm had}\bigg], \tag{4.22}$$

without the $1/m_W^2$ suppression of (4.21). Therefore it can be of similar size as (4.21) when the chemical potentials are small. n_{ν_α} and n_{e_α} are particle minus anti-particle number densities of neutrinos and charged leptons. They can be written in terms of the particle chemical potentials μ_i,

$$n_i = \chi_i\mu_i, \tag{4.23}$$

where the lepton susceptibilities χ_i can be evaluated in the ideal gas limit,

$$\chi_{e_\alpha} = -2g_{e_\alpha}\int\frac{d^3p}{(2\pi)^3}f'_{\rm F}(E_\alpha), \tag{4.24}$$

$$\chi_{\nu_\alpha} = g_{\nu_\alpha}\frac{T^2}{6}, \tag{4.25}$$

with $g_{\nu_\alpha} = 1$, $g_{e_\alpha} = 2$. The hadronic contribution to the electric charge density $n_Q^{\rm had}$ can be written as

$$n_Q^{\rm had} = \chi_{QQ}^{\rm had}\mu_Q + \chi_{QB}\mu_B, \tag{4.26}$$

where $\chi_{QQ}^{\rm had}$ is the hadronic contribution to the electric-charge susceptibility. The particle chemical potentials in (4.23) can be written in terms of the chemical potentials of the slowly varying and of the conserved charges,

$$\mu_{e_\alpha} = \mu_{L_\alpha} - \mu_Q, \tag{4.27}$$

$$\mu_{\nu_\alpha} = \mu_{L_\alpha}. \tag{4.28}$$

The latter can be expressed through the lepton number densities n_{L_α} by inverting

$$n_B = \chi_{BB}\mu_B + \chi_{QB}\mu_Q, \tag{4.29}$$

$$n_Q = \left(\chi_{QQ}^{\text{had}} + \chi_{QQ}^{\text{lep}}\right)\mu_Q + \chi_{QB}\mu_B + \chi_{QL_\alpha}\mu_{L_\alpha}, \tag{4.30}$$

$$n_{L_\alpha} = \chi_{L_\alpha L_\alpha}\mu_{L_\alpha} + \chi_{QL_\alpha}\mu_Q, \tag{4.31}$$

and assuming vanishing overall baryon and electric charge density, $n_B = n_Q = 0$. Concretely, this yields the expressions

$$\mu_B = -\frac{\chi_{BQ}}{\chi_{BB}}\mu_Q, \tag{4.32}$$

$$\mu_{L_\alpha} = \frac{n_{L_\alpha} - \chi_{QL_\alpha}\mu_Q}{\chi_{L_\alpha L_\alpha}}, \tag{4.33}$$

$$\mu_Q = \frac{\sum_\alpha \frac{\chi_{QL_\alpha}}{\chi_{L_\alpha L_\alpha}} n_{L_\alpha}}{\frac{\chi_{BQ}^2}{\chi_{BB}} + \sum_\alpha \frac{\chi_{QL_\alpha}^2}{\chi_{L_\alpha L_\alpha}} - \chi_{QQ}}. \tag{4.34}$$

Plugging them into (4.22) gives us functions c_α that are linear in the asymmetries n_{L_α}, with coefficients determined by susceptibilities.

The leptonic part of the electric charge susceptibility in (4.30) can be written in terms of (4.24),

$$\chi_{QQ}^{\text{lep}} = \sum_{\alpha=e,\mu,\tau} \chi_{e_\alpha}. \tag{4.35}$$

The susceptibilities in (4.31) are related to (4.24),(4.25) by

$$\chi_{L_\alpha L_\alpha} = \chi_{e_\alpha} + \chi_{\nu_\alpha}, \tag{4.36}$$

$$\chi_{QL_\alpha} = -\chi_{e_\alpha}. \tag{4.37}$$

The susceptibilities χ_{QQ}^{had}, χ_{BQ}, and χ_{BB} have been determined on the lattice for temperatures near the QCD crossover [98, 99]. Reference [62] has used a hadron resonance gas model below and perturbation theory above and connected all three regions via spline interpolations, which we are going to use.[1]

4.3.2 Imaginary parts

The dominant contribution to the imaginary part of the active-neutrino self-energy, i.e., the opacity Γ_α, appears at $\mathcal{O}(G_F^2)$ since the $\mathcal{O}(G_F)$ contributions are suppressed by $\exp(-m_W/T)$. The corresponding diagram is shown in figure 4.2. The opacity can be split into a leptonic and a hadronic piece,

$$\Gamma_\alpha = \Gamma_\alpha^{\text{lep}} + \Gamma_\alpha^{\text{had}}. \tag{4.38}$$

[1] Available at `https://github.com/ntveem/sterile-dm/tree/master/data/tables`.

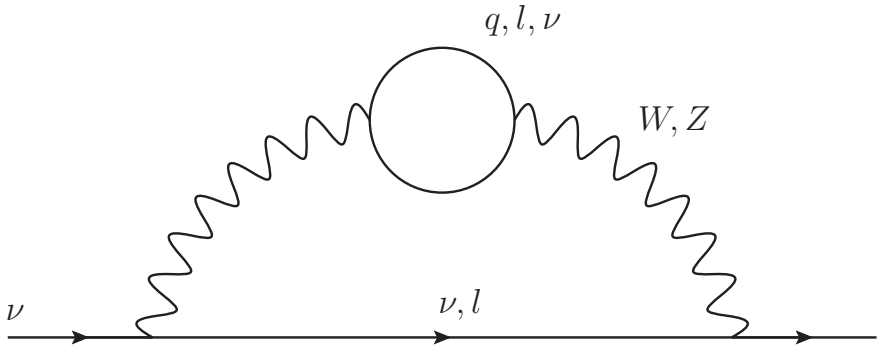

Figure 4.2: Two-loop diagram contributing to the active-neutrino opacity (4.38). Quarks in the upper loop can only be treated perturbatively at temperatures way above the QCD crossover.

The leptonic part can be computed perturbatively by simply considering a free lepton-antilepton pair in the top loop, since leptons basically behave like free particles at temperatures much below the electroweak scale. Over a large part of the temperature range which is relevant for sterile neutrino production, $\Gamma_\alpha^{\mathrm{had}}$ is non-perturbative. Two different approaches have been taken to calculate this function. In [97], the free-quark approximation is used for the whole temperature range, but in order to account for the strong interaction, the number of colors N_c is replaced by a temperature dependent $N_{c,\mathrm{eff}}(T)$ which vanishes at low temperatures, and equals 3 at the highest temperature. In [62], on the other hand, the free-quark approximation at high temperatures is connected to chiral perturbation theory at low temperatures via spline interpolations. We refer to these two approximations for (4.38) as $\Gamma_\alpha^{N_{c,\mathrm{eff}}}$ and $\Gamma_\alpha^{\mathrm{spline}}$. We will also consider the approximation $\Gamma_\alpha^{\mathrm{had}} = 0$ for which we write Γ^{lep}.

We show the different muon-flavor opacities in figure 4.3 for a fixed energy. With increasing temperature, the leptonic opacity slightly increases due to crossings of the muon and tau mass thresholds. When the temperature reaches m_μ or m_τ respectively, these particles can be produced on-shell and thus populate the plasma, which naturally increases the neutrino opacity. In contrast, the hadronic opacity contributions rise more strongly when increasing the temperature through the QCD crossover. As hadronic bound states melt during this process, the number of on-shell degrees of freedom (which also interact weakly) rises strongly, which is why $\Gamma^{N_{c,\mathrm{eff}}}$ and Γ^{spline} increase. The small rise of Γ^{spline} at low temperatures is a signature of the onset of processes like two- and three-body fusions involving broad resonances from the hadron resonance gas model [62].

The opacity is an important ingredient of the active-neutrino spectral function and therefore for sterile neutrino production. Moreover, it is the least known ingre-

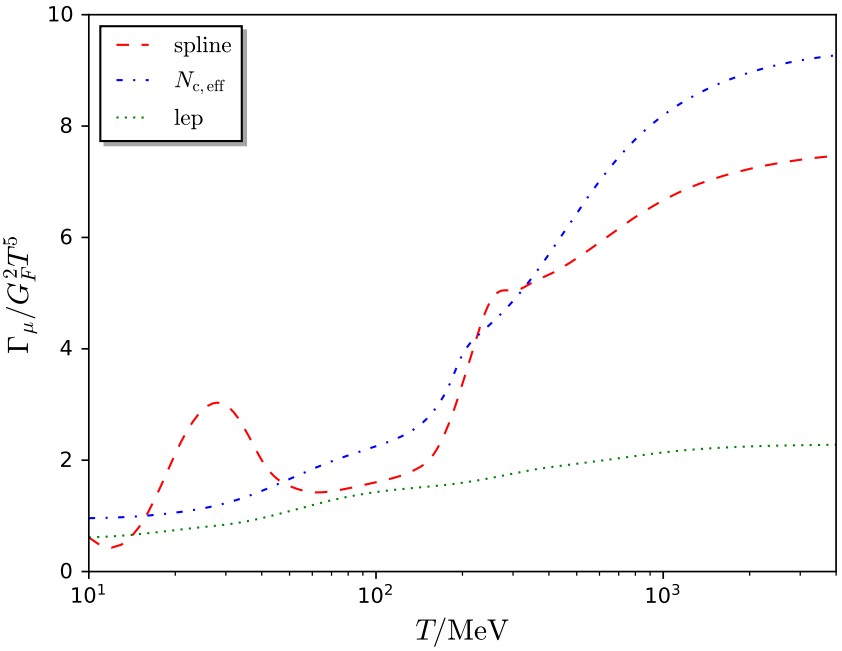

Figure 4.3: The three different opacities as functions of temperature for energy $k^0 = T$.

dient. But with the above approximations at hand, we can investigate its influence on different sterile neutrino dark matter scenarios with and without lepton asymmetries. This is what we will do in the following chapter.

Chapter 5

Impact of active-neutrino opacities

5.1 Non-resonant production

5.1.1 Setup

As a starting point for studying hadronic opacity contributions, this chapter deals with the case of non-resonant sterile neutrino production. For that case, we do not consider any non-zero initial lepton asymmetries and (4.6) is set to zero. Moreover, no chemical potentials appear in (4.5) and the active-neutrino self-energy contribution (4.22) vanishes, $c_\alpha = 0$. The remaining real part of the self-energy, (4.21), does not have any hadronic contributions at leading order in the weak coupling. They only arise at two-loop order and are neglected. The only hadronic self-energy contribution we are left with, is the opacity Γ^{had} in (4.38).

In this setup, both the positive and negative helicity phase space densities in (4.5) will evolve equally in time, given that (4.12) and (4.13) are equal at leading order in $M/|\mathbf{k}|$. We set $f_{\mathbf{k}-} = f_{\mathbf{k}+} \equiv f_{\mathbf{k}}$ and only track the evolution of $f_{\mathbf{k}}$, simply multiplying the final density by a factor 2 to obtain the complete abundance. We make the simplifying assumption that only one Yukawa coupling is non-zero, namely h_μ. Then only the term with $\alpha = \mu$ contributes in (4.5). This allows us to compare the effect of the opacities $\Gamma_\alpha^{N_{\text{c,eff}}}$, which are available for all three lepton flavors, and $\Gamma_\alpha^{\text{spline}}$, which is currently only available for $\alpha = \mu$. We integrate (4.5) from $T = 4$ GeV down to 10 MeV, outside of this range the right-hand side is vanishingly small and no sterile neutrino production takes place. The opacities $\Gamma_\mu^{\text{spline}}$ and Γ_μ^{lep} are available for momenta $10^{-4} \leq |\mathbf{k}|/T \leq 20$, whereas $\Gamma_\mu^{N_{\text{c,eff}}}$ is available for $0.03 \leq |\mathbf{k}|/T \leq 12.5$. We use the latter range when solving the evolution equations, which is sufficient for our purposes. We will always be using the parameterizations of the energy density $\rho(T)$ and entropy density $s(T)$ as well as the speed of sound

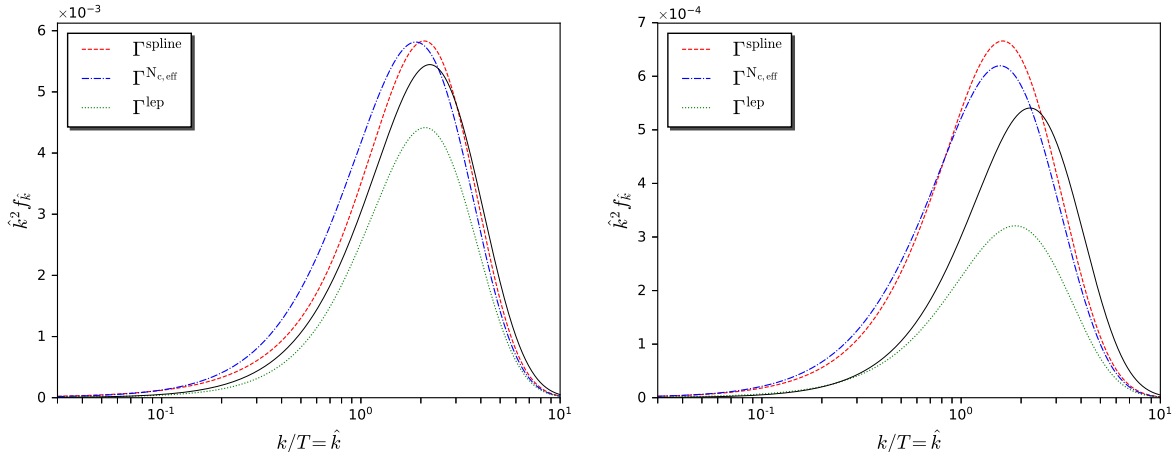

Figure 5.1: Solutions to (4.5) at $T = 10$ MeV for two different combinations of mass and mixing angle, without any lepton asymmetry. Left: $M = 1$ keV, $\sin^2(2\theta) = 6.8 \cdot 10^{-8}$, right: $M = 10$ keV, $\sin^2(2\theta) = 10^{-9}$. The three colored curves correspond to the use of the three different opacities. For each mass, the mixing angle was chosen such that the resulting energy density roughly gives the dark matter abundance for the highest curve. The fractions of the dark matter energy density read: left: $(\Omega_s/\Omega_{DM})_{spline} = 1.003$, $(\Omega_s/\Omega_{DM})_{N_{c,eff}} = 0.986$, $(\Omega_s/\Omega_{DM})_{lep} = 0.755$, right: $(\Omega_s/\Omega_{DM})_{spline} = 1.012$, $(\Omega_s/\Omega_{DM})_{N_{c,eff}} = 0.938$, $(\Omega_s/\Omega_{DM})_{lep} = 0.529$ respectively. The solid black lines are Fermi-Dirac distributions with an overall suppression factor chosen such that their energy densities give the relic abundance.

$c_s(T)$ from [97] [1], based on calculations in [94].

5.1.2 Results

We compare the resulting sterile neutrino phase space densities at $T = 10$ MeV obtained with the different opacities $\Gamma_\mu^{spline}, \Gamma_\mu^{N_{c,eff}}$, and Γ_μ^{lep}. We show results with exemplary parameter values in figure 5.1. We find that the use of Γ_μ^{spline} leads to the most efficient production, closely followed by $\Gamma_\mu^{N_{c,eff}}$ with a difference in final abundances below the 10% level, for the masses we consider. The purely leptonic opacity is the smallest one, leading to the lowest curve and the least efficient production with a final abundance between 25% and 50% smaller than with the highest curve. The mixing angle $\sin^2(2\theta)$ dictates the absolute abundances but does not influence their relative differences. The specific choices for figure 5.1 roughly lead to the relic dark matter abundance for the red curve but beyond that, they are completely arbitrary and can be adjusted to give any fraction of the dark matter abundance.

[1] Available at `www.laine.itp.unibe.ch/dmpheno/release_2016jun21.tar.gz`.

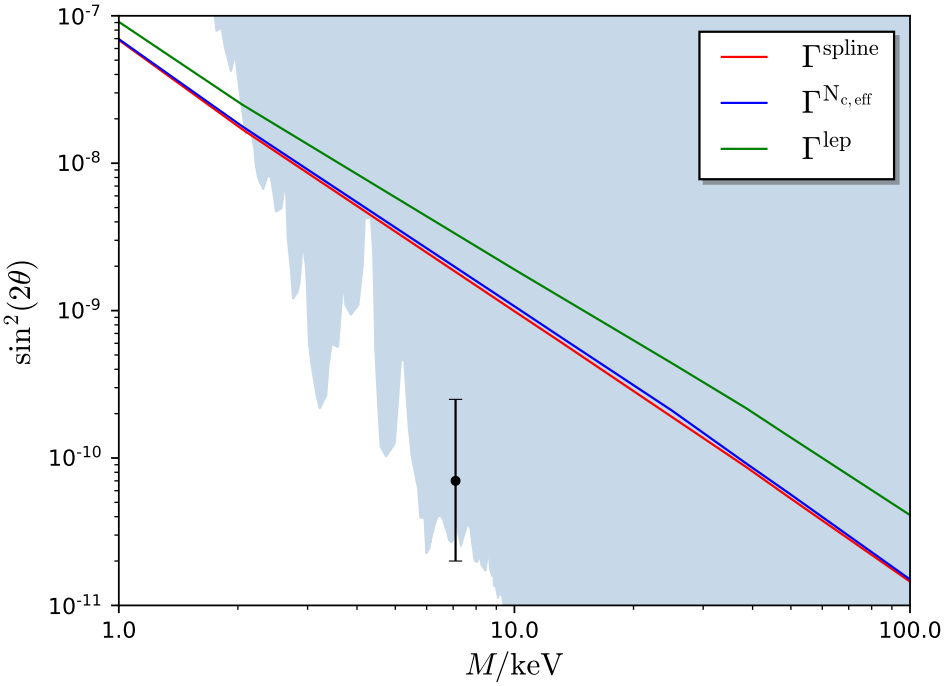

Figure 5.2: Parameter values for which the relic dark matter abundance is produced, $\Omega_s = \Omega_{\mathrm{DM}}$. The three lines correspond to the use of the three different opacities. The shaded region is excluded by X-ray constraints taken from [22], see also [107–110]. The tentative 3.5 keV signal is indicated by the black dot, the error bar corresponds to the uncertainty in the measured line intensity, cf. section 3.2.2.

Figure 5.1 hints at the fact that the higher the mass, the lower does the green curve lie beneath the other two curves. Since the two full opacities differ most from the leptonic opacity in the region of the highest considered temperatures (cf. figure 4.3), we expect from (1.2) that for higher sterile neutrino masses, the relative differences in the final phase space densities increase as the production is shifted towards higher temperatures. In figure 5.2, we show lines of constant sterile neutrino abundance in the (M, $\sin^2(2\theta)$) - parameter space for a large range of masses. The X-ray constraints are already very strong and only allow for low masses $M \lesssim 2$ keV if we require sterile neutrinos to give the full dark matter abundance. For such low masses however, the resulting spectra are reasonably close to a thermal form, which is represented by the black curves in figure 5.1. For example, in the left plot, the mean momenta of the three colored curves are roughly 10% lower than the mean momentum of the thermal spectrum, which leads to very strong lower mass bounds from structure formation, cf. section 3.3.2. Furthermore, we see that when using the two full opacities, one requires very similar mixing angles to produce the same

abundance. The blue curve is slightly above the red one, with differences in the mixing angle below the 10%-level for all masses. With the leptonic opacity, the mixing angle has to be much higher than with the other two opacities. The green curve lies higher than the blue curve by ∼30% for the lowest shown masses and by up to 180% for the highest masses. This is in accordance with the fact that the production is shifted towards higher temperatures upon increasing the mass. Then the full opacities become significantly larger than the leptonic opacity, resulting in a boosted production and in turn a smaller, required mixing angle. Generally, we find that the hadronic contributions play a notable role in sterile neutrino production, even though the uncertainties do not exceed the 10%-level when comparing Γ^{spline} to $\Gamma^{N_{c,\text{eff}}}$. Still, it can be concluded that a precise determination of non-resonant sterile neutrino production rates requires a more precise determination of the involved hadronic opacity. This might be desired for models that assume not all but a sizable portion of dark matter to be composed of sterile neutrinos.

5.2 Resonant production

5.2.1 Setup

We have seen that the hadronic opacity is relevant for non-resonant production of sterile neutrinos and a precise, non-perturbative determination in the future is desirable. In this chapter we check its relevance for resonant production, which is a viable sterile neutrino dark matter scenario. Producing the complete dark matter abundance requires quite large lepton asymmetries, which can lead to resonances. Thus, we now need to solve the coupled system of equations (4.5) and (4.6). Again, we limit ourselves to $\alpha = \mu$. Then only the muon-flavor asymmetry will be dynamical. In principle, non-zero electron and tau-flavor asymmetries can influence the evolution equations as they appear in the functions c_α, but we assume these to be zero unless specified otherwise.

We choose $M = 7.1$ keV and $\theta_\mu^2 = 2.5 \cdot 10^{-13}$ as a representative point in the available parameter space. The conclusions we will draw from our results will be independent of that choice. We compare the resulting sterile neutrino phase space densities at $T = 10$ MeV obtained with the different opacities $\Gamma_\mu^{\text{spline}}, \Gamma_\mu^{N_{c,\text{eff}}}$, and Γ_μ^{lep} for a set of different positive initial values for n_{L_μ}/s. For positive lepton asymmetries, resonances mainly contribute to the production of sterile neutrinos with negative helicity, while for positive helicity the resonant contribution is suppressed with $M/|\mathbf{k}|$. If there are resonances, then there are usually two resonance frequencies for each $|\mathbf{k}|$ [19,62,63]. For most of the relevant temperatures, the two resonances lie in the momentum range we consider. In practice, the smaller resonance frequency dominates the sterile neutrino dark matter production, and the larger one plays a

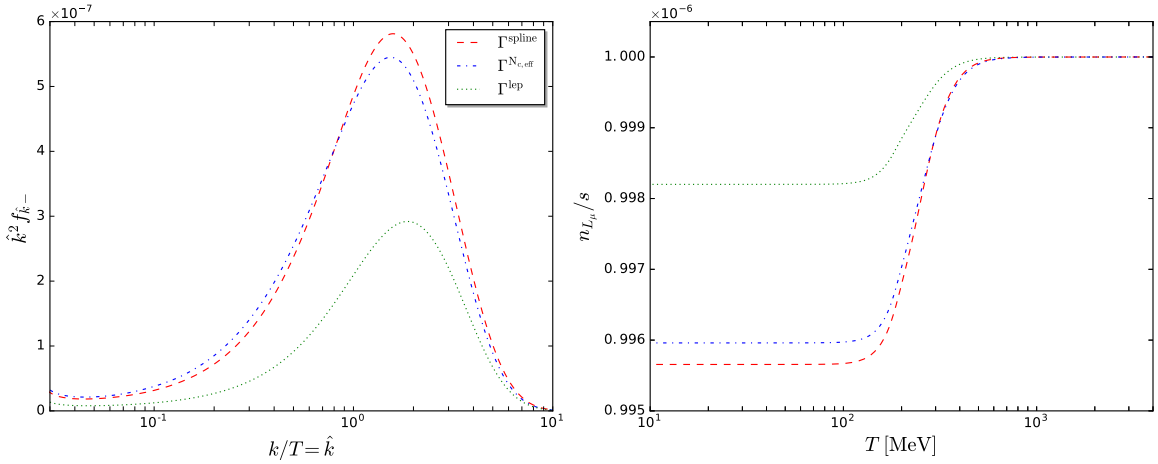

Figure 5.3: Solutions to the kinetic equations for $M = 7.1\text{keV}$, $\theta_\mu^2 = 2.5 \cdot 10^{-13}$. The different curves are obtained with the different approximations for Γ_α. Left: Phase space densities of sterile neutrinos with negative helicity at $T = 10$ MeV. The fraction of the dark matter energy density is $(\Omega_\text{s}/\Omega_\text{DM})_\text{spline} = 5.7 \cdot 10^{-4}$, $(\Omega_\text{s}/\Omega_\text{DM})_{N_{c,\text{eff}}} = 5.3 \cdot 10^{-4}$, $(\Omega_\text{s}/\Omega_\text{DM})_\text{lep} = 3.2 \cdot 10^{-4}$ respectively. Right: Evolution of the lepton asymmetry.

negligible role [62].

5.2.2 Results

We show results for three different initial values of n_{L_μ}/s in figures 5.3, 5.4 and 5.5, additional ones can be found in appendix A. Generally we observe that the higher the initial lepton asymmetry, the larger the phase space densities become. In figure 5.3, the lepton asymmetry is so low that resonances are outside the displayed momentum range (the dominant one leads to the slight increase at small momenta) and only give a small contribution to the production. In contrast, the initial lepton asymmetry in figure 5.4 is high enough so that each momentum mode in the shown range passes through a resonance, giving much larger phase space densities. The same is true for figure 5.5, where we chose the initial asymmetry such that we obtain the complete dark matter abundance. In figure 5.3, we see how the different approximations for the opacity influence the sterile neutrino production and in parallel the depletion of n_{L_μ}/s. The purely leptonic contribution is the smallest one, resulting in the least efficient production. In figures 5.4 and 5.5, one can see that for a larger initial lepton asymmetry, there is only a sub-percent difference in the final abundance of sterile neutrinos between using the full opacity and using only the leptonic contribution. The resulting phase space densities have become indistinguishable. In the limit $\Gamma_\alpha \to 0$, (4.12) turns into a delta function [63]. This indicates that the

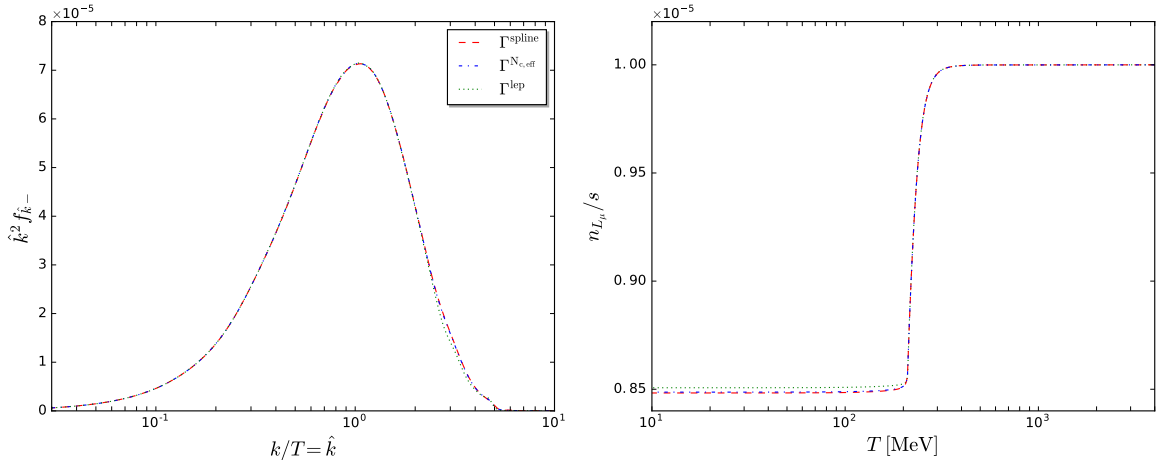

Figure 5.4: Same as figure 5.3 but with a higher initial lepton asymmetry. The fraction of the dark matter energy density in all three cases is roughly $\Omega_s/\Omega_{DM} = 2.5 \cdot 10^{-2}$.

dominant resonance in figures 5.4 and 5.5 is so sharply peaked, that the differences in the active-neutrino opacities become irrelevant. The same is true for the lepton asymmetry evolution. No matter what opacity is used, the depletion is almost identical. We find that this behavior occurs in all of the allowed (white) parameter space shown in figure 6.2, if we tune the lepton asymmetry such that the resulting sterile neutrino energy density gives the correct dark matter abundance. The differences in energy densities obtained with the different opacities are typically below the 2% level, for very low masses and high mixing angles at most 5%. The transition from quite different to basically equivalent solutions by increasing the lepton asymmetry can be followed in smaller steps in appendix A.

We have used the publicly available code of [63] to check our calculation, and what we find is mostly in agreement with our results described above. For very high asymmetries we find that the resulting phase space densities suffer from sporadic kinks, hinting at numerical instabilities which we could not get rid of by naively increasing the desired precision. Nevertheless the resulting figures resemble ours quite well.

Our findings partly disagree with the ones in [62], which were calculated using *sterile-dm*, a publicly available code created by the authors of [62]. It uses 1,000 momentum bins as a default, which apparently misses parts of the resonances in the sterile neutrino production. While this problem is absent for non-resonant production, it becomes more and more severe for increasing asymmetry. We have explicitly checked that increasing the number of momentum bins to 30,000 gives results which mainly agree with ours. This problem could be the cause of the rather large differ-

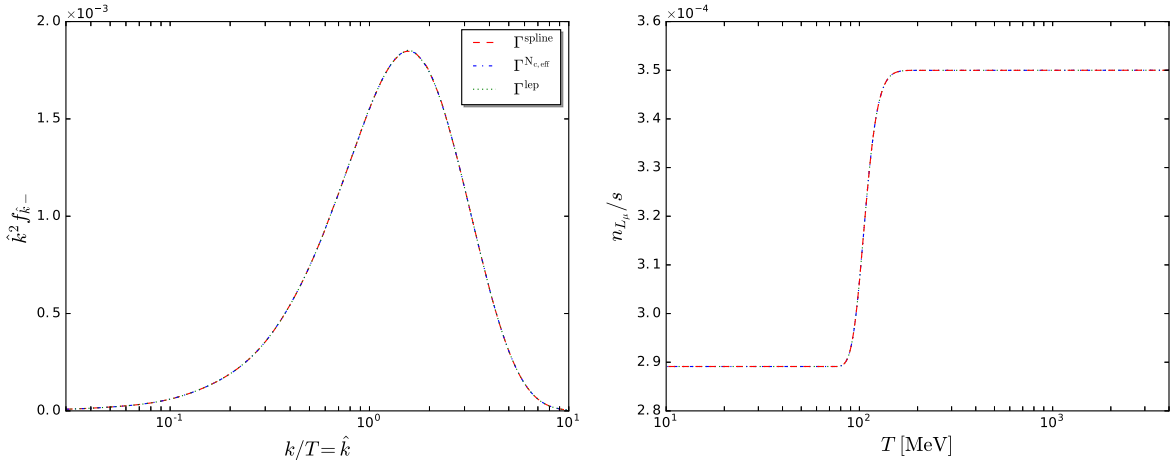

Figure 5.5: Same as figure 5.3 but with an initial lepton asymmetry tuned such that the sterile neutrino energy density gives the complete relic dark matter abundance, $\Omega_{\rm s} = \Omega_{\rm DM}$.

ences in the phase space densities using either $\Gamma_\alpha^{N_{c,\rm eff}}$ or $\Gamma_\alpha^{\rm spline}$ which was observed in [62].

The lepton asymmetries needed to produce the complete dark matter abundance ($\Omega_{\rm s}/\Omega_{\rm DM} = 1$) are quite large compared to the baryon asymmetry. Most baryogenesis mechanisms produce comparable amounts of lepton and baryon asymmetries before electroweak sphaleron freeze-out. In the νMSM [111], which contains two additional heavier sterile neutrinos, a larger lepton asymmetry can be produced thereafter [112, 113]. However, it turns out this can boost the lepton asymmetry by at most a factor 1,000 [114], and that one can reach at most $\Omega_{\rm s}/\Omega_{\rm DM} = 1/10$ [101]. In this scenario, improving on calculations for hadronic contributions to active-neutrino opacities can be important [101], as the lepton asymmetries are even smaller than in figure 5.3.

Chapter 6

Parameter constraints for resonant production

Efficient sterile neutrino production via resonances can provide the dark matter abundance with much smaller mixing angles than in the non-resonant case. However, the required lepton asymmetries cannot be arbitrarily high due to observational constraints from BBN and the CMB, which we introduced in section 3.3.4. We compute new, lower limits on the active-sterile mixing angle in accordance with these upper limits on the lepton asymmetry. We will summarize the results in a parameter plot with all relevant limits. They will also include lower mass limits from Lyman-α observations, which we do not calculate ourselves, but we can confirm them based on a numerical comparison to other studies.

6.1 Lower mixing angle bounds from BBN and CMB

We start this section by computing the lower limits on the mixing angle from BBN and the CMB, for which one can obtain $\Omega_\mathrm{s}/\Omega_\mathrm{DM} = 1$. We separately use both (3.36) and (3.37) for that purpose. For simplicity, we take these maximal values as initial conditions at $T = 4$ GeV. The lepton asymmetry at times prior to the onset of BBN could be higher, as long as it is depleted enough during sterile neutrino production. However, the depletion turns out to be only on the level of a few percent for the low mixing angles considered here. We calculate, for various masses, the mixing angle that leads to the complete relic dark matter abundance. The only non-zero neutrino Yukawa coupling is h_μ. The results are given in table 6.1, displaying the scenario where all asymmetry is in the muon flavor (left) and the scenario where the asymmetry is split equally onto all three flavors (right).

As we have seen in section 5.2, our calculations generally give larger phase space densities than *sterile-dm*, if it is used for resonant production "as is" with 1,000 default momentum bins. This code was used to calculate the BBN limit in [69, 110,

Table 6.1: Mixing angle that leads to the complete relic dark matter abundance for various masses, with total initial asymmetry $n_L/s = 2.5 \cdot 10^{-3}$ (BBN limit) or $n_L/s = 1.2 \cdot 10^{-2}$ (CMB/BBN limit). Left: asymmetry only in the muon flavor, right: all three asymmetries initially equal, $n_{L_\alpha}/s = n_L/3s$.

M/keV	$\sin^2(2\theta) \cdot 10^{13}$	
	BBN	CMB/BBN
1	30	6
2	11	2.2
5	2.8	0.6
10	1.03	0.24
20	0.39	0.09
50	0.12	0.025
70	0.08	0.016

M/keV	$\sin^2(2\theta) \cdot 10^{13}$	
	BBN	CMB/BBN
1	47	10
2	16	3.7
5	4.1	0.99
10	1.48	0.39
20	0.57	0.15
50	0.20	0.04
70	0.14	0.026

115, 116], giving much stronger limits than the ones we find, especially for the lower end of the mass range in table 6.1. Again, increasing the number of momentum bins, *sterile-dm* gives better agreement with our results. On the other hand we note that our BBN limits are in closer agreement with the only slightly lower ones in [13], which are also displayed in [109, 117], and also with the ones shown in [118], which are based on [87].

The limits we obtain from the CMB measurements are much weaker than the ones from BBN alone. They can be classified as much more robust than the pure BBN limits as they do not suffer from such large systematic uncertainties (cf. section 3.3.4). Therefore, we stick to these limits for the final parameter space plot in section 6.3.

One has to keep in mind that the used bounds only apply to the total lepton asymmetry. In fact, n_{L_μ} could be larger than (3.36) or (3.37) if it is partly compensated by the other lepton flavor asymmetries. But the same compensation would not take place in (4.22), where the different flavors enter with different coefficients. Therefore c_μ would increase, leading to a larger production rate and to a weaker bound on $\sin^2(2\theta)$.

6.2 Lower mass bounds from the Lyman-α forest

In contrast to the scenario of non-resonant sterile neutrino production, where the resulting spectra do not deviate too strongly from a thermal form for low masses, resonant production can lead to much colder spectra. In figure 6.1, we show the mean momenta of our final spectra for a large range of masses and mixing angles. The colormap is an interpolation between values calculated on a grid covering the

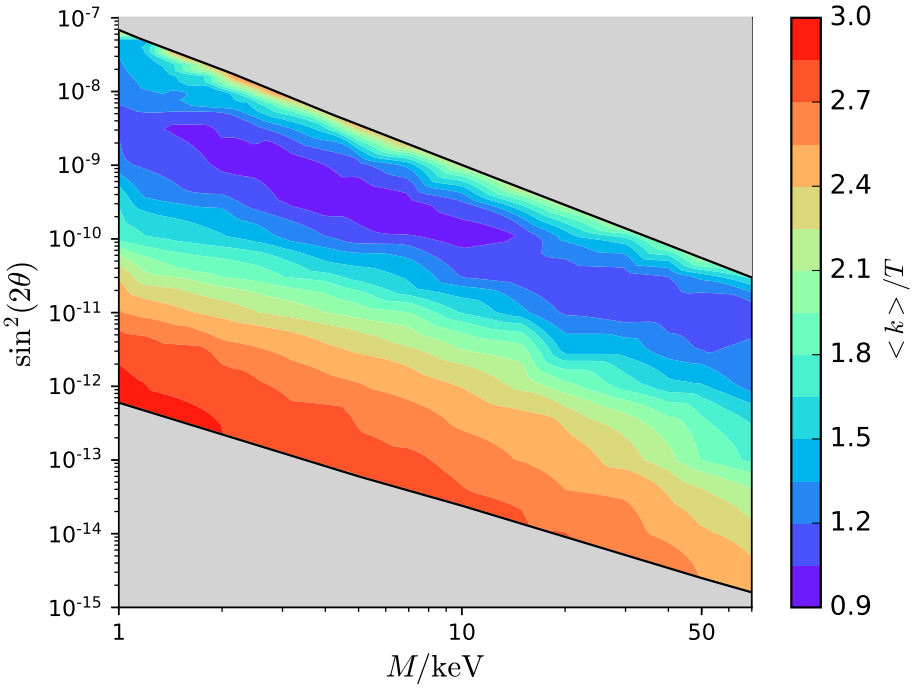

Figure 6.1: Mean momenta of sterile neutrino distributions at $T = 10$ MeV which give the relic dark matter abundance, $\Omega_s = \Omega_{\rm DM}$. The boundaries to the excluded (grey) regions correspond to zero (upper region) and maximal (lower region) lepton asymmetry, the latter corresponds to the BBN/CMB bound from table 6.1 (left). The shown range of masses and mixing angles covers all of the allowed parameter space when combining all relevant constraints, which are shown explicitly in section 6.3.

shown parameter space. For each point on the grid, the relic dark matter abundance is reached by adjusting the lepton asymmetry accordingly. The mean momentum is a suitable feature to look at in order to get an idea of how different from a thermal shape the final spectra can turn out if one fixes the mass, the mixing angle and the final abundance. We generally find colder than thermal spectra in the entire parameter space shown (for a Fermi-Dirac distribution $\langle k \rangle / T \simeq 3.15$). For mixing angles roughly an order of magnitude lower than the upper limit, one needs a moderate amount of lepton asymmetry, typically $n_{L_\mu}/s \sim 10^{-6} - 10^{-4}$, in order to produce the dark matter abundance. This moderate amount leads to resonant enhancements of the low momentum modes, but keeps high modes untouched. This results in very cold distributions (blue shaded regions). For decreasing mixing angles, higher lepton asymmetries are needed, $n_{L_\mu}/s \gtrsim 10^{-4}$, which let resonances extend also towards higher momentum modes. Hence, the distributions become warmer

again (orange/red shaded regions).

Overall, we expect that structure formation bounds from Lyman-α observations should become much weaker here than for non-resonant production. Their application in the first place also becomes more difficult, since mass limits cannot be estimated from limits on thermal relics as done in section 3.3.2. Instead, one requires a dedicated calculation of power spectra involving the explicit distribution functions in order to obtain limits on the free-streaming scales, which then constrain the mass. Such a calculation is done in [119], using the distribution functions produced by the Mathematica code of [63]. We already used that code to confirm what we found in section 5.2 and found well agreeing distribution functions for a large range of initial lepton asymmetries. Therefore, we conclude that the derived constraints from [119] apply here as well. The result is a lower mass limit excluding masses below ~ 7 keV for almost all mixing angles $\sin^2(2\theta) \gtrsim 10^{-13}$, which is considerably stronger than the limit from phase space analysis. We expect the limit to continue to lower mixing angles, but this is not shown in [119] and thus we do not have access to it in this region. We show the explicit limit together with all previously introduced parameter constraints in section 6.3.

Similar calculations have been performed, e.g., in [115,116] using the distribution functions that are produced by the code *sterile-dm*. We generally find colder spectra than [116], with a mean momentum that is typically between 25% and 50% lower, depending on the region in the parameter space. The Lyman-α limits shown in [116] are much stronger than the ones displayed in [119], excluding the entire parameter space. Due to the already mentioned issues regarding *sterile-dm*, we conclude that these limits are too strong.

6.3 Combined constraints

In the final section of this chapter, we provide a new plot in which we summarize all parameter constraints on resonantly produced sterile neutrino dark matter that we discussed so far. Besides constraints from X-ray and Lyman-α observations as well as phase space density analysis, which we did not compute ourselves, we add new constraints from CMB/BBN. Our results, together with the constraints introduced in chapter 3, are shown in figure 6.2. The allowed region (white space) is bounded from all sides. For very high active-sterile mixing angles, sterile neutrino production can result in too much dark matter abundance even without any lepton asymmetry. This overproduction region is shown as the green-shaded area. Non-resonant production of the relic dark matter density can take place on the boundary of that region (upper solid black line), which corresponds to the Dodelson-Widrow scenario. We have used the active-neutrino opacity $\Gamma_\mu^{\text{spline}}$ (cf. section 4.3.2) for all

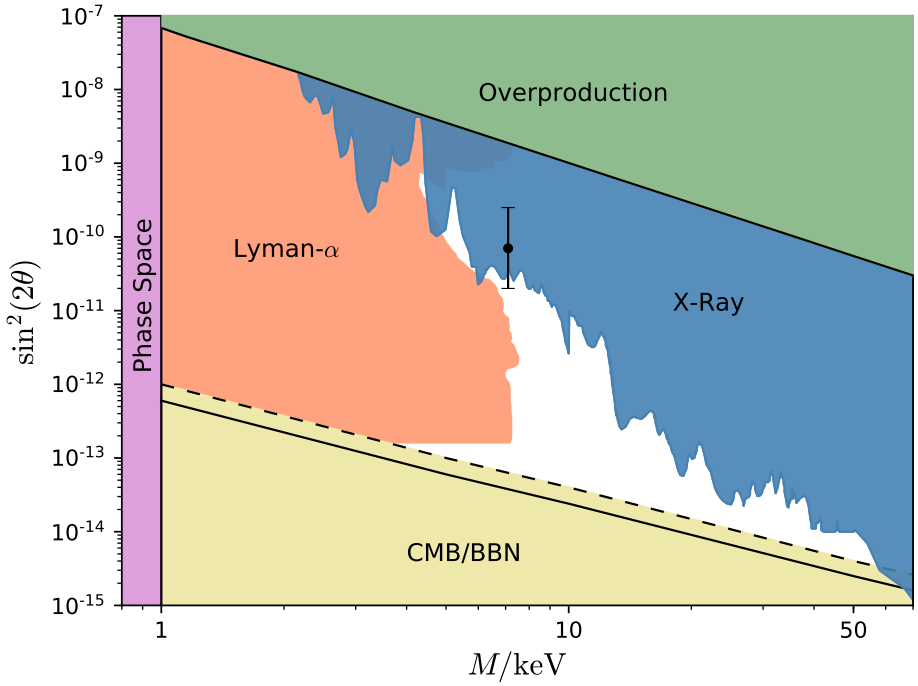

Figure 6.2: Combined constraints for keV sterile neutrino dark matter that is resonantly produced with the help of a lepton asymmetry. The X-ray constraints are taken from [22], see also [107–110]. Phase space density constraints are from [64]. The Lyman-α limits are taken from [119]. The CMB/BBN limit given by the solid black line holds if all of the input lepton asymmetry is only in the muon flavor. The dashed line corresponds to the CMB/BBN limit if the input lepton asymmetry is split equally onto all three flavors. The tentative 3.5 keV signal is indicated by the black dot.

calculations here, which really only affects the location of that black line slightly, see figure 5.2. Below the region of overproduction, resonance effects due to non-zero lepton asymmetries make this choice irrelevant and using one of the other opacities $\Gamma_\mu^{N_{\mathrm{c,eff}}}$ and $\Gamma_\mu^{\mathrm{lep}}$ would not change anything then.

We were able to weaken previous, lower limits on the mixing angle from BBN. Combining the lower limit on the mixing angle from BBN alone (BBN column in table 6.1) with X-ray constraints, closes the available parameter space for masses $M \gtrsim 40$ keV, which is not shown here. Still, this leaves us with more free space than previous studies [69, 110, 115, 116]. The lower limits from the CMB and BBN (CMB/BBN column in table 6.1) lead to a closing of the available parameter space for $M \gtrsim 70$ keV when combined with X-ray constraints, which is why we did not calculate limits for even higher masses. The CMB/BBN limits are more robust than

from BBN alone, which is the reason we show them here. With these new limits on the mixing angle, we were able to open up the parameter space for resonant production of sterile neutrino dark matter considerably.

In section 6.2, we found that the Lyman-α limits calculated in [119] apply here since they are based on basically the same sterile neutrino distribution functions as the ones we calculated. These limits take away a lot of the otherwise allowed parameter space as they are much stronger than the lower mass limits from phase space arguments. Nevertheless, they do not reach up to $M = 7.1$ keV and therefore the sterile neutrino interpretation of the 3.5 keV line signal remains viable. In the upper mixing angle range, there is a horn-like dip in the Lyman-α excluded region, where slightly lower masses are possible. A feature of that sort does not come unexpected, since the corresponding sterile neutrino spectra turn out especially cold in that region (cf. figure 6.1), leading to large free-streaming wavelengths and thus weak structure formation limits.

Chapter 7

Enhanced production from self-interacting neutrinos

Primordial lepton asymmetries are very weakly constrained and can help in producing large amounts of sterile neutrinos via resonant production. This gives a viable dark matter scenario but the available parameter space is quite restricted and could shrink further in the future due to, e.g., upcoming X-ray observations. Also the question about the origin of such large lepton asymmetries is left open.

In this chapter, we investigate a simple alternative in which no lepton asymmetries are required for efficient production via active-sterile mixing, while parameter constraints are also much weaker. The price for that is having to introduce additional field content beyond the SM. A minimal working extension is provided by the simple addition of a new scalar field, which mediates self-interactions among the active neutrinos. These self-interactions give contributions to the active-neutrino spectral functions, which can significantly increase the sterile neutrino production. This model relies on the same production mechanism as the original Dodelson-Widrow scenario, only with an altered production rate. This is different from the possibly more known scenario of sterile neutrino production via decay of heavy scalars, which does not rely on active-sterile mixing, see, e.g., [120]. There exist rather weak observational constraints on the scalar field mass and coupling, which will translate to a much wider, available sterile neutrino parameter space for producing the relic dark matter density than in the last chapter. Furthermore, we will see that the interactions of the new field with the active neutrinos can in principle lead to resonances, just like non-zero lepton asymmetries do. Similar to what we did in the last chapter, our goal here will be understanding the importance of resonances and the role of opacities for this dark matter scenario. This new scenario was originally proposed in [22], where the appearance of resonance effects was mentioned but no deeper investigation, other than referring to them as accidental, took place. We will clarify the situation and see what impact resonances have in this scenario.

7.1 Contribution to active-neutrino self-energy

We consider a model in which self-interactions among active neutrinos assist in producing sterile neutrino dark matter. For that purpose, we extend the Lagrangian (4.1) by adding a new complex scalar field ϕ which couples to active neutrinos ν_α, with the interaction

$$\mathcal{L}^{\phi}_{\text{int}} = \sum_{\alpha,\beta} \frac{\lambda_{\alpha\beta}}{2} \phi \, \nu_\alpha \nu_\beta + \text{h.c.} \tag{7.1}$$

In order to preserve SM gauge invariance, such an interaction can be obtained from a higher dimensional operator,

$$\mathcal{L}^{\phi}_{\text{int}} = \phi \frac{(l_\alpha \widetilde{\varphi})(l_\beta \widetilde{\varphi})}{\Lambda_{\alpha\beta}} + \text{h.c.} \tag{7.2}$$

with the cutoff scale $\Lambda_{\alpha\beta}$. This results in (7.1) after electroweak symmetry breaking, $\langle \widetilde{\varphi} \rangle = (v/\sqrt{2}, 0)^\top$, with the dimensionless coupling $\lambda_{\alpha\beta} = v^2/\Lambda^2_{\alpha\beta}$. This effective operator can be derived from a renormalizable theory at higher energy scales [121]. We will only be interested in phenomenological implications of the interaction (7.1) from here on. For simplicity, we assume non-zero coupling only for muon-flavor neutrinos, so only the terms with $\alpha = \beta = \mu$ contribute in the following. Moreover, the only remaining coupling $\lambda_{\mu\mu}$ will be denoted by λ from here on.

The self-energy (4.10) of active muon-flavor neutrinos receives additional contributions from the new field. We write the real and imaginary parts as

$$b_\mu = b^{\text{SM}}_\mu + b^{\phi}_\mu, \tag{7.3}$$

$$\Gamma_\mu = \Gamma^{\text{SM}}_\mu + \Gamma^{\phi}_\mu, \tag{7.4}$$

where the first terms are the SM contributions introduced in chapter 4, (4.21) and (4.38) respectively. The new scalar field contributions carry the superscript ϕ. Since we do not assume any non-zero lepton asymmetries in this chapter, the function c_μ in (4.10) is zero. The contribution b^{ϕ}_μ to the self-energy comes from the real part of the same one-loop graph shown in figure 4.1 on the left, only that the gauge field line is replaced by a scalar field line. For a general scalar mass m_ϕ, we find

$$b^{\phi}_\mu = \frac{\lambda^2}{16\pi^2 k^2} \int_0^\infty dp \left[\left(\frac{m^2_\phi p}{2\varepsilon} L_2(p,k) - \frac{4kp^2}{\varepsilon} \right) f_B(\varepsilon) + \left(\frac{m^2_\phi}{2} L_1(p,k) - 4kp \right) f_F(p) \right] \tag{7.5}$$

with the energy $\varepsilon = \sqrt{p^2 + m^2_\phi}$ and the logarithmic functions

$$L_1(p,k) = \ln\left(\frac{m^2_\phi + 4kp}{m^2_\phi - 4kp} \right), \tag{7.6}$$

$$L_2(p,k) = \ln\left(\frac{m_\phi^2 + 2k(w+p)}{m_\phi^2 + 2k(w-p)}\right) + \ln\left(\frac{m_\phi^2 - 2k(w-p)}{m_\phi^2 - 2k(w+p)}\right). \tag{7.7}$$

This agrees with the result of [122] in the limit of vanishing fermion mass. Expression (7.5) takes simple forms for very high or very low temperatures. For $T \gg m_\phi$, the logarithmic terms can be dropped and we are left with the asymptotic form

$$b_\mu^\phi = -\frac{\lambda^2 T^2}{16k}, \tag{7.8}$$

whereas in the limit $T \ll m_\phi$, expanding the logarithms to leading order in p/m_ϕ gives [123, 124]

$$b_\mu^\phi = \frac{7\pi^2\lambda^2 k T^4}{90 m_\phi^4}. \tag{7.9}$$

It is important to note that, when going from high to low temperatures, b_μ^ϕ changes its sign. It is negative in the high-temperature regime, where it may compensate the positive b_μ^{SM}, such that resonances in the spectral function (4.11) can occur in principle. The necessary parameters for creating sizable resonance effects in sterile neutrino production, if they exist in the first place, have to be determined numerically.

The imaginary part of the same one-loop diagram gives the leading opacity contribution Γ_μ^ϕ, at least for intermediate scalar masses, $m_\phi \lesssim T$. For such masses, neutrinos interact mainly through the decay and inverse decay of on-shell ϕ particles. We find the expression

$$\Gamma_\mu^\phi = \frac{\lambda^2 m_\phi^2 T}{8\pi k^2}\left[\ln\left(1 + e^{m_\phi^2/(4kT)}\right) + \frac{k}{T} - \ln\left(e^{m_\phi^2/(4kT)+k/T} - 1\right)\right], \tag{7.10}$$

which slightly differs from the corresponding expression in [22], although they coincide for large momenta k. A detailed calculation of our result is presented in appendix B. The opacity (7.10) becomes very small in the limit $m_\phi \gg T$, just like the SM opacity is exponentially suppressed at leading order in the coupling due to very heavy gauge bosons. Then the leading scalar field contribution is obtained from two-loop order and reads [22]

$$\Gamma_\mu^\phi = \frac{7\pi k \lambda^4 T^4}{864 m_\phi^4}. \tag{7.11}$$

In numerical evaluations, we consider scalar field masses in the range $1\,\mathrm{MeV} \leq m_\phi \lesssim T_{\max} = 4\,\mathrm{GeV}$ (cf. section 7.2 for the lower limit), which is sufficient for our purposes of investigating effects on dark matter and resonances. Then expression (7.11) plays only a minor role when we solve the sterile neutrino evolution equations. We have checked that, as stated in [121], it is a very good numerical approximation to use the sum of (7.10) and (7.11) over the whole temperature range when solving the sterile neutrino evolution equations.

7.2 Parameter constraints

If the new scalar particles are light enough and in thermal equilibrium with the active neutrinos, they can lead to an enhanced expansion rate of the Universe during BBN, which would alter the formation of light elements. Additionally they decay into active neutrinos at later times, leading to an enhanced N_{eff} with measurable impacts on the CMB. In [125], it is shown that for sizable couplings, a lower mass limit is necessary to ensure that the scalar particle density is Boltzmann-suppressed enough to be in accordance with predictions of light element abundances from BBN. They report

$$m_\phi > 5.2\,\text{MeV for } \lambda \gtrsim 10^{-4}. \tag{7.12}$$

For weaker couplings, the limits should be relaxed. References [126, 127] suggest

$$m_\phi \gtrsim \mathcal{O}(0.1)\,\text{MeV for } \lambda \gtrsim 10^{-8}, \tag{7.13}$$

relying on BBN predictions as well as on CMB measurements. The regime of even lower couplings is not subject to any notable BBN limits.

Besides observational constraints related to the cosmology of the early Universe, there also exist constraints on self-interactions of active neutrinos in the laboratory. In case of a scalar mediator, the strongest constraints come from the search of rare meson decays, primarily from the kaon decay $K^+ \to \mu^+\bar{\nu}_\mu\nu\nu$ [121]. The pair of neutrinos emerges from the decaying scalar, $\phi \to \nu\nu$. The lower limit on the branching ratio $\text{Br}(K^+ \to \mu^+\bar{\nu}\nu\nu) > 2.4 \cdot 10^{-6}$ [128] for this decay results in an upper limit on the coupling $\lambda_{\mu\mu}$ for intermediate masses $m_\phi \lesssim \mathcal{O}(100)$MeV. For increasingly higher masses, the limit becomes weaker as the decay becomes more suppressed. Both, the BBN limit and the kaon decay limit are shown in figure 7.1.

7.3 Numerical results

Our numerical evaluations will ensue like in chapter 5. We solve the sterile neutrino evolution equations (4.5) by integrating over T and again, we limit ourselves to the case of h_μ being the only non-zero Yukawa coupling between active and sterile neutrinos. Besides the SM contributions, the active-neutrino self-energy now also contains contributions from the scalar field and so we use (7.3), (7.4) in the spectral function (4.11). We will stick to using $\Gamma_\mu^{\text{spline}}$ (cf. section 4.3) as the SM-input to (7.4) from here on. As it turns out, the opacity contribution Γ_μ^ϕ is much larger and thus dominating, rendering the specific choice of the SM opacity irrelevant. This statement holds true for values of m_ϕ and λ that are necessary for yielding the relic dark matter abundance. Since the self-energy contributions from the scalar field are affecting both sterile neutrino helicity states equally, unlike a non-zero lepton

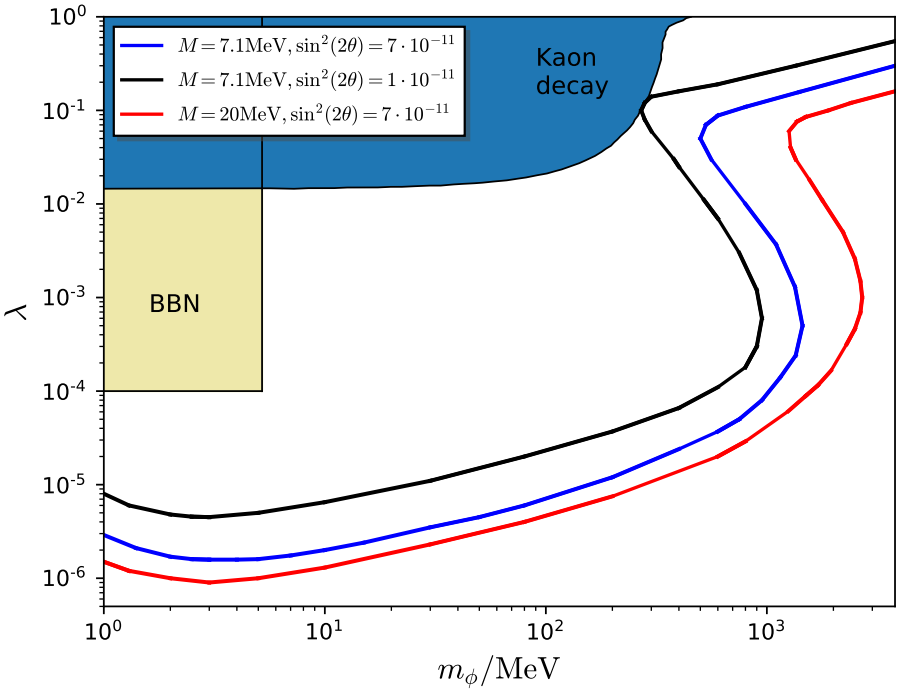

Figure 7.1: Locations in the parameter space of the ϕ-field where the produced sterile neutrinos make up all of the dark matter, $\Omega_s = \Omega_{\text{DM}}$, given fixed values of M and $\sin^2(2\theta)$. The three lines correspond to exemplary choices of the latter. The relic dark matter abundance is produced anywhere on the lines. Parameter constraints are indicated by the color-shaded regions. The BBN constraint is from [125], the constraint from kaon decay is from [121].

asymmetry with a fixed sign, we can track the evolution of only one helicity and multiply the resulting abundance by 2. In contrast to the previous chapters, where the production rate typically runs inefficient not too far below T_{QCD}, we find that the rate can be large also for lower temperatures down to $T \sim \mathcal{O}(1\,\text{MeV})$, due to the large opacity Γ_μ^ϕ. Therefore, we choose 1 MeV as the lower end of the T-integration range instead of 10 MeV. We cannot go to lower temperatures as we do not have numerical values for entropy and energy density at hand there.

7.3.1 Parameter values for the relic abundance

We begin by fixing points in the $(M, \sin^2(2\theta))$-plain and exploring how the scalar field impacts the production of sterile neutrinos. In figure 7.1, we show a large range of values of m_ϕ and λ which are necessary for obtaining the relic dark matter density, given three different sets of sterile neutrino parameters. For each set, there exists an

infinite amount of combinations of such m_ϕ and λ values, which continuously connect to form the "S"-shaped lines shown. We choose $M = 7.1$ keV and $\sin^2(2\theta) = 7 \cdot 10^{-11}$ as exemplary parameters (blue line), corresponding to the central values for the tentative 3.5 keV-line signal. By altering either M (red line) or $\sin^2(2\theta)$ (black line), we can see how m_ϕ and λ have to be adjusted to keep the relic density unchanged. Generally, a higher sterile neutrino mass or a higher mixing angle both increase the production rate and require a smaller λ for fixed m_ϕ. Besides slightly altering the shape of the lines, this moves the whole line towards the bottom-right direction in that plane. In contrast, a lower sterile neutrino mass or mixing angle tends to move the lines to the upper-left.

The location of the blue line agrees very well with the location of the corresponding line shown in [22], which uses the same parameters. Only towards the lower end of the m_ϕ-range we find slight differences. Our line bends up towards higher λ-values when ϕ is decreased below ~ 5 MeV, while it continues to go straight down in [22]. This difference probably comes from the fact that for low m_ϕ, the sterile neutrino production becomes efficient towards low temperatures and we only integrate down to 1 MeV, while the authors of [22] integrate down to 0.1 MeV. Thus, it appears that we are not able to cover all of the relevant production temperatures and in turn require slightly higher λ to compensate that. However, a complication in that regard arises due to the decoupling of active neutrinos which typically takes place in this temperature regime. On the one hand, the applicability of the evolution equations (4.5) is no longer justified when the active neutrinos fall out of thermal equilibrium. On the other hand, the new self-interactions should keep them in equilibrium longer than in the SM scenario. A detailed calculation, taking these effects into account, goes beyond the scope of the work presented in this thesis but could be interesting for future investigations. We do not consider masses $m_\phi \lesssim 5$ MeV in the following and so we do not expect this issue to be relevant from here on.

7.3.2 Resonance effects and opacity impact

As a next step, we want to see where resonance effects come into play and how relevant they are. Resonances occur when the square bracket in the denominator of the spectral function (4.11) becomes very small. Even though we do not have any lepton asymmetries here and thus $c_\mu = 0$, we found in section 7.1 that resonances are possible in the regime $T \gg m_\phi$ due to a negative b_μ^ϕ. Their location and strength is different for each momentum mode and temperature and also depends on the values of the parameters M, m_ϕ and λ. The mixing angle $\sin^2(2\theta)$ only influences the overall abundance. We have fixed $M = 7.1$ keV and scanned most of the allowed parameter space shown in figure 7.1, searching for resonance signatures in the form of peaks in the phase space densities. We checked only the region $m_\phi < 1$ GeV,

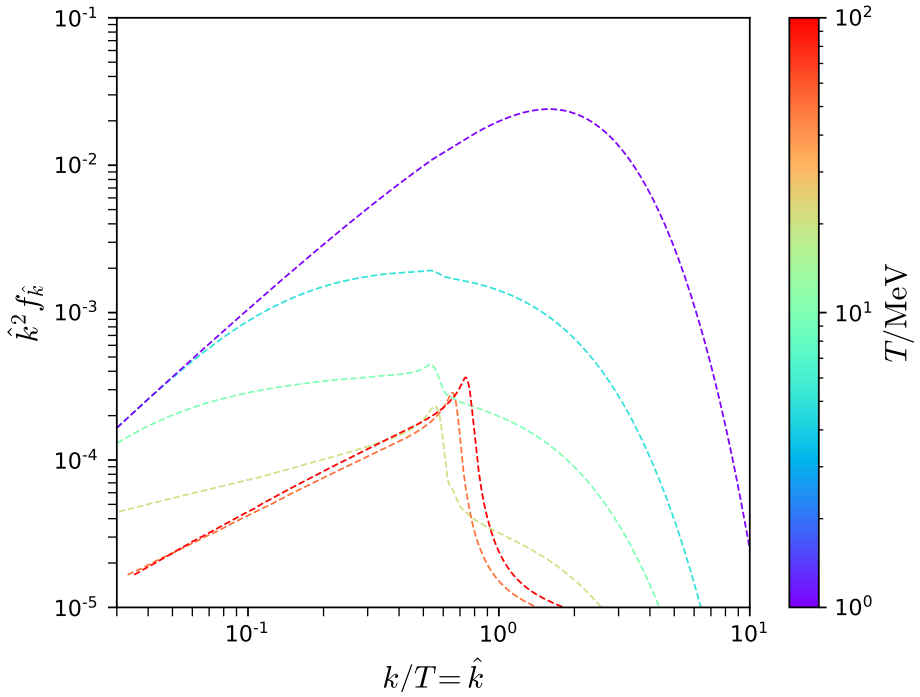

Figure 7.2: Solution to the evolution equations for $M = 7.1$ keV, $\sin^2(2\theta) = 10^{-12}$, $m_\phi = 5$ MeV, $\lambda = 7.5 \cdot 10^{-5}$ at different temperatures.

since resonances only occur for $m_\phi \ll T$ and the sterile neutrino production rate is generally very small at temperatures above 1 GeV. We did not find any peaks in the densities at the final temperature $T_{\text{end}} = 1$ MeV, however we were able to find them at higher temperatures. In figure 7.2, we show the temperature evolution of the sterile neutrino phase space density for $m_\phi = 5$ MeV and $\lambda = 7.5 \cdot 10^{-5}$, a combination of values that turns out to give well pronounced peaks. At $T = 100$ MeV, the density shows a clear peak at $k \sim 0.8T$ (red curve). Around that momentum mode, resonant production has visibly contributed to the phase space density evolution down to this temperature. Going further down to $T = 50$ MeV (orange curve), the shape of the density barely changes as the production has run inefficient by then. The slight shrinking of the curve is due to redshifting momenta. The following steps in temperature (curves shown explicitly at $T/\text{MeV} = 20, 10, 5, 1$) show how the production rate increases again, significantly populating every momentum mode in the shown range. This increase is however due to the large opacity (7.10), driving non-resonant production. The resonance peak is overshadowed in that process and becomes less and less significant as the temperature decreases, down to the point where it is no longer visible. We have not explicitly tracked the temperature evolution of the phase space density in all available regions of figure 7.1, but we

expect that resonances occur in more instances than the one shown in figure 7.2. Nevertheless, none of them contribute notably to the final densities, as we could not find remnants of resonance peaks in any of them. This can be contrasted to our findings in section 5.2. There we found that once resonances occur in sterile neutrino production, the corresponding momentum modes evolve only due to resonance effect and the non-resonant contribution is negligible, shown by the fact the the choice of the opacity does not play a role anymore. Here, resonances can occur but their effect on the final spectrum is overshadowed by efficient non-resonant production due to the high opacity contribution Γ_μ^ϕ. We conclude that resonance effects are negligible for this sterile neutrino production scenario.

7.3.3 Sterile neutrino parameter space

Last but not least, we want to see how the new self-interactions among active neutrinos influence the available parameter space for sterile neutrino dark matter. The large opacity contribution enhances the production rate compared to the Dodelson-Widrow scenario, which should allow for smaller active-sterile mixing angles to be viable. From figure 7.1 we get a glimpse of how a lower bound on the mixing angle can be established. For a fixed sterile neutrino mass M, a lower mixing angle leads to a shift of the line of constant abundance towards the upper left (going from the blue to the black line). In practice, lowering the mixing angle eventually leads the line to completely submerge into the excluded, color-shaded regions. The lowest, viable mixing angle is given by the requirement that some part of the line is still in the allowed region just in front of the BBN-excluded region and simultaneously below the region excluded by kaon decay. We do not consider values $\lambda \gtrsim 1$ as this extends beyond the perturbative realm.

For a given mass M, we have determined the value for λ that gives the highest possible abundance along the BBN line $m_\phi = 5.2$ MeV and then reduced the mixing angle $\sin^2(2\theta)$ such that we end up with the correct abundance. The resulting lower limit is shown in figure 7.3. We find a very weak lower limit on the mixing angle in comparison to the CMB/BBN limit in figure 6.2. This gives us a lot of available parameter space, which closes only shortly before $M = 1$ GeV. For higher M, we either produce not enough dark matter or run into X-ray constraints. On the one hand, our available space reaches to slightly higher values for M than in [22], where slightly stronger limits meet the same X-ray constraints already around $M \approx 700$ MeV. On the other hand, their limit is slightly weaker for the lower M-range. We assume these differences to arise due to slightly different results for the opacity Γ_μ^ϕ, different endpoints in the temperature integration range, or a mixture of both. In contrast to the non-resonant and resonant production scenarios without additional field content, no Lyman-α constraints have been computed for this scenario so far.

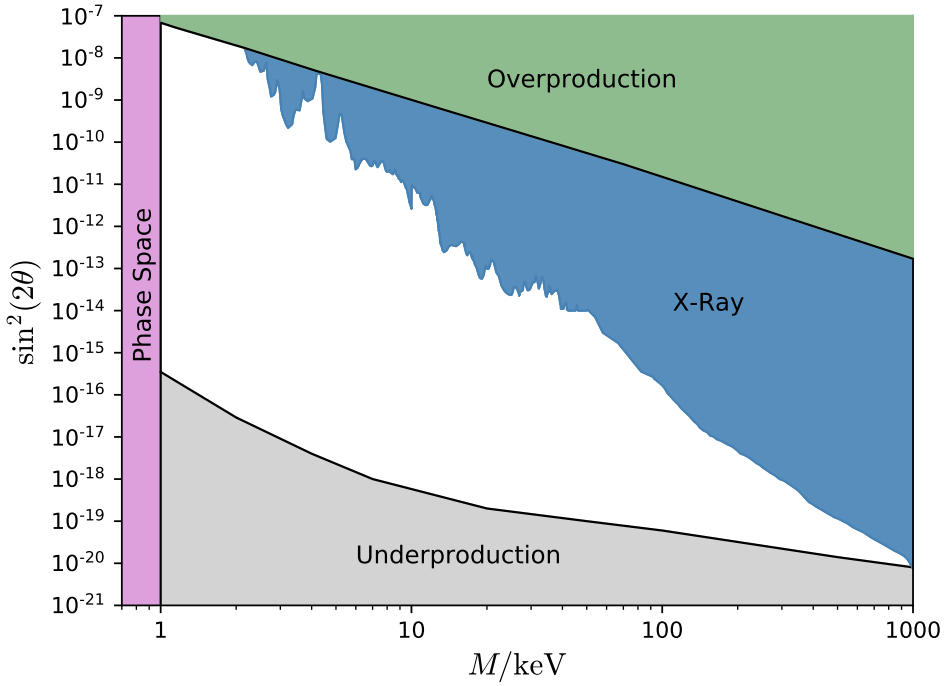

Figure 7.3: Combined constraints for keV sterile neutrino dark matter that is produced in the presence of a new scalar field, mediating self-interactions among active neutrinos. The X-ray constraints are taken from [22], see also [70, 107–110]. Phase space density constraints are from [64]. In the grey region, no allowed combinations of the scalar field parameters m_ϕ and λ could be found that would lead to the production of the relic dark matter abundance.

Their computation is especially difficult here since at each available point in the sterile neutrino parameter space, there are many different scalar field parameters leading to the relic abundance. The different combinations generally result in sterile neutrino spectra with different shapes and mean momenta, which could affect structure formation in different ways. All in all, we find that this simple scalar field extension of the SM can significantly impact the production of sterile neutrino dark matter, with very weak parameter constraints compared to the scenario of resonant production via lepton asymmetries.

Chapter 8

Summary and conclusions

Sterile neutrinos with masses on the keV-scale represent a theoretically well-motivated candidate for dark matter. Due to their mixing with active neutrinos, they are produced from the thermal plasma in the early Universe. This process takes place mainly during the QCD epoch, where strong-interaction effects can play an important role but are difficult to compute at the same time. In this thesis, we have investigated how non-resonant and resonant production scenarios are affected by active-neutrino opacities, which are the largest source of hadronic uncertainties. Furthermore, we provide the most up-to-date available parameter space for resonantly produced sterile neutrino dark matter by calculating new limits on the mixing angle, based on BBN and observations of the CMB. We also studied a model in which new self-interactions among active neutrinos can help in making the production more efficient, as an alternative to large lepton asymmetries.

In chapter 5, we solve coupled evolution equations of sterile neutrino phase space densities and lepton number densities using different approximations for the active-neutrino opacity as input. The three approximations model the hadronic input in different ways and by comparing their influence on the final phase space densities and resulting dark matter abundances, we can estimate the importance of strong-interaction effects.

We first consider non-resonant production in section 5.1, where no lepton asymmetry is present. In that case, we find that hadronic opacity contributions are substantial. For very low sterile neutrino mass, $M = 1$ keV, the purely leptonic opacity $\Gamma^{\rm lep}$ gives roughly 20-25% less abundance than the two full opacities $\Gamma^{\rm spline}$ and $\Gamma^{\rm N_c,eff}$. This difference only becomes larger when M increases and it is independent of the mixing angle $\sin^2(2\theta)$, the latter only controlling the absolute abundances. The differences in abundance between using $\Gamma^{\rm spline}$ or $\Gamma^{\rm N_c,eff}$ are generally around 10% or below. For the low mass range, we find that the resulting spectra resemble thermal spectra quite well, with similar mean momenta. This confirms the applicability of lower mass bounds from Lyman-α forest observations, which together with

X-ray constraints on the mixing angle, exclude the sterile neutrinos in this scenario from providing all of the dark matter. However, if they are only required to make up a fraction of the dark matter abundance or if one introduces, e.g., additional sterile flavors, this scenario remains viable. Then, non-perturbative determinations of the hadronic opacity contributions would be desirable for precise computations of sterile neutrino abundances.

In section 5.2, we introduce a non-zero lepton asymmetry which boosts the sterile neutrino production via resonances. For lepton asymmetries as high as $n_{L_\alpha}/s \gtrsim 10^{-6}$, necessary for producing the complete dark matter abundance and at the same time avoiding strong parameter constraints from Lyman-α and X-ray observations, we find that the hadronic opacity plays no role in the production anymore. The sharp resonances dominate the production process and no distinction between the uses of the three opacities Γ^{spline}, Γ^{lep} and $\Gamma^{\text{N}_\text{c},\text{eff}}$ can be made. We conclude that non-perturbative input in the form of hadronic opacities will not be necessary in this scenario. Still, strong-interaction effects play a role as they also enter the equation of state and the real part of the active-neutrino self-energy. However, these effects are under much better control as lattice QCD calculations have already been incorporated.

We were able to confirm our findings with the two publicly available codes for resonant sterile neutrino production, a Mathematica code from [63] and *sterile-dm* [62]. While substantially different results were produced by *sterile-dm* at first, we could identify an inaccuracy in that code and successfully resolve the discrepancy by adjusting the numerical precision.

In chapter 6, we present parameter constraints on resonantly produced sterile neutrino dark matter. The code *sterile-dm* was used previously to calculate lower limits on the mixing angle $\sin^2(2\theta)$ from BBN [69, 110, 115, 116], which we were able to update. We find much weaker limits, especially for low masses, which provides more available parameter space for that scenario than in these previous studies. Furthermore, we have calculated similar limits based on limits derived from the CMB [88], which are in accordance with BBN. They have not been used before in the context of sterile neutrino dark matter. They are much weaker than the limits from BBN alone but come with much smaller, systematic uncertainties. Lyman-α constraints on the sterile neutrino mass have been calculated for the resonant production scenario [119], using phase space densities produced by the Mathematica code associated with [63]. Our calculations give very similar densities, which allows us to incorporate the same Lyman-α constraints in our work. In figure 6.2, we summarize the relevant constraints on resonantly produced sterile neutrino dark matter, providing a new parameter exclusion plot.

Finally, chapter 7 deals with a slightly different scenario in which sterile neutrino dark matter is efficiently produced with the help of a new scalar field ϕ that

mediates self-interactions among active neutrinos. Through its contributions to the active-neutrino self-energy, the scalar field can strongly amplify sterile neutrino production. We consider masses $m_\phi \lesssim T$, which can result in the appearance of resonances through a negative contribution to the real self-energy. We have calculated the opacity contribution and find that it is very large and dominates the SM contributions. The latter arise at a higher loop level due to high gauge boson masses. We find that the large opacity renders resonance effects irrelevant for the final sterile neutrino abundances. Non-resonant production, being very efficient down to the lowest temperature $T = 1$ MeV we consider, overshadows resonances completely. This behavior is the opposite of what we found in chapter 5 about resonant production through large lepton asymmetries. There, opacities are comparatively small and resonances completely dominate the production process.

We find that the relic dark matter abundance is easily produced in this scenario, since the scalar field mass and coupling are rather weakly constrained. For fixed sterile neutrino parameters, we find the correct abundance on continuous lines in the scalar field parameter space, which are mainly in accordance with the results in [22]. We find small deviations for very low scalar field masses, which could be due to differences in the opacity and the the fact that we were only able to take temperatures $T \geq 1$ MeV into account, ending one order of magnitude earlier than [22]. While this implies that we could have missed some parts of the effective production range, the validity of the evolution equations in this range is not clear at the same time. Based on existing constraints on the scalar field parameters, we finally calculated a lower limit on the active-sterile mixing angle. The available space for sterile neutrino parameters turns out quite large as a result. We find a slightly stronger limit than [22] for the lower end of possible sterile neutrino masses, but a slightly weaker limit for very high masses, with allowed regions up to $M \sim 1$ GeV for mixing angles $\sin^2(2\theta) \sim 10^{-20}$.

Appendix A

Emergence of resonances with increasing lepton asymmetries

Here we show the negative helicity phase space densities and corresponding lepton asymmetries like in figures 5.3 - 5.5, comparing the use of the three different opacities. The sterile neutrino parameters are $M = 7.1\text{keV}$, $\theta_\mu^2 = 2.5 \cdot 10^{-13}$ in all shown cases. From top to bottom we gradually increase the initial lepton asymmetry (figures on the right), whereby the resonances extend more towards higher momentum modes (figures on the left). When a mode passes through a resonance, it becomes blind to the choice of the active-neutrino opacity.

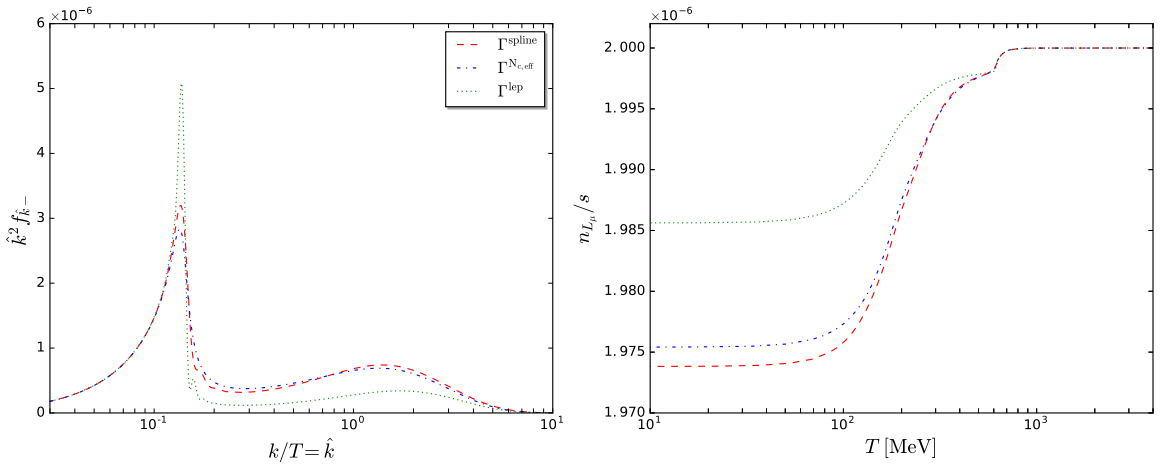

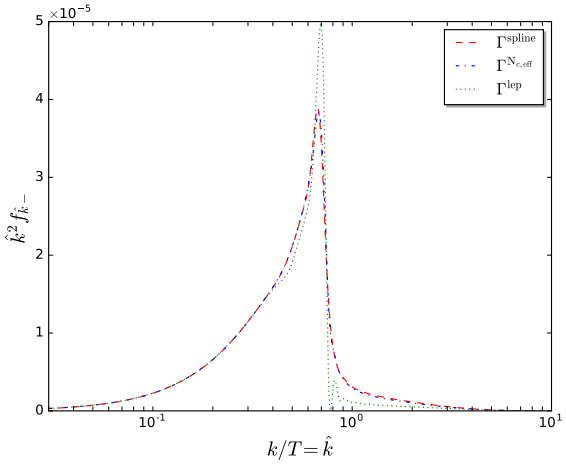
$\times 10^{-5}$
$\Gamma^{\rm spline}$
$\Gamma^{\rm N_{c,eff}}$
$\Gamma^{\rm lep}$
$\hat{k}^2 f_{\hat{k}-}$
$k/T = \hat{k}$

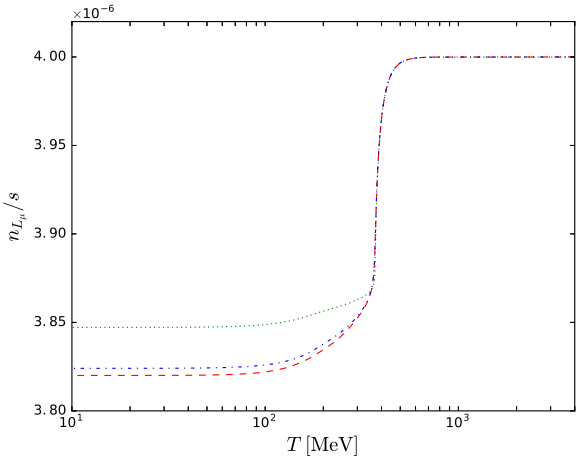
$\times 10^{-6}$
n_{L_μ}/s
T [MeV]

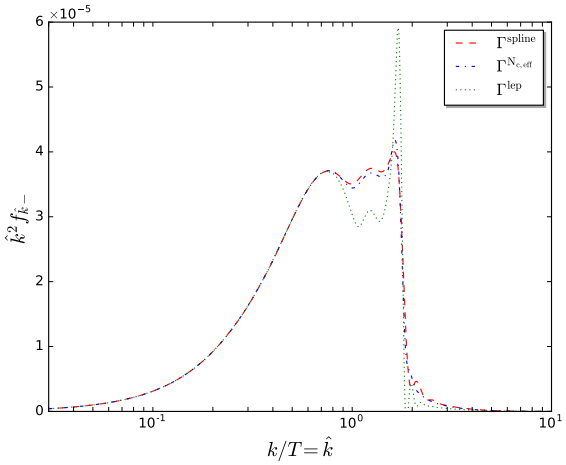
$\times 10^{-5}$
$\Gamma^{\rm spline}$
$\Gamma^{\rm N_{c,eff}}$
$\Gamma^{\rm lep}$
$\hat{k}^2 f_{\hat{k}-}$
$k/T = \hat{k}$

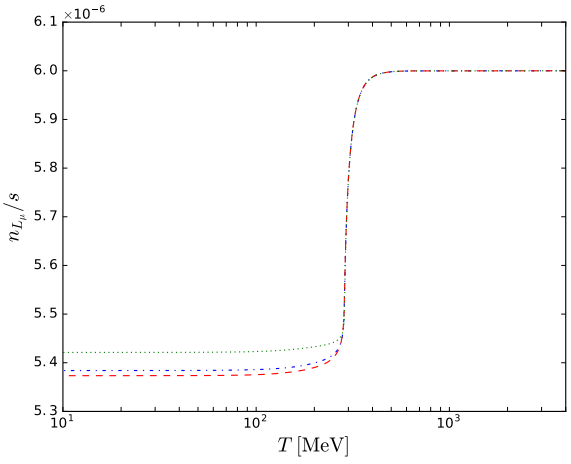
$\times 10^{-6}$
n_{L_μ}/s
T [MeV]

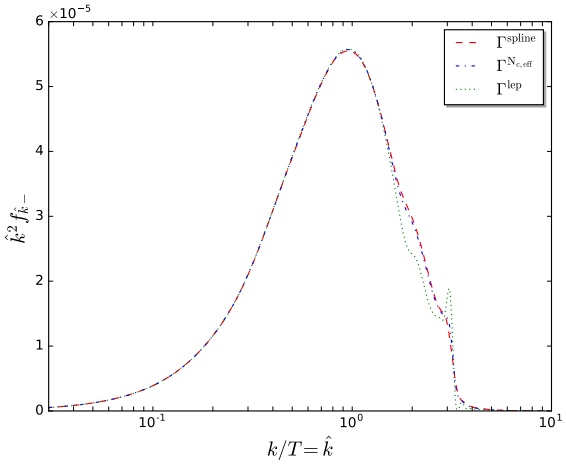
$\times 10^{-5}$
$\Gamma^{\rm spline}$
$\Gamma^{\rm N_{c,eff}}$
$\Gamma^{\rm lep}$
$\hat{k}^2 f_{\hat{k}-}$
$k/T = \hat{k}$

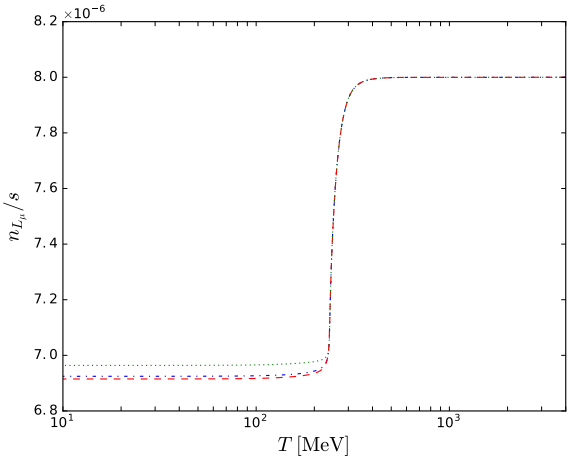
$\times 10^{-6}$
n_{L_μ}/s
T [MeV]

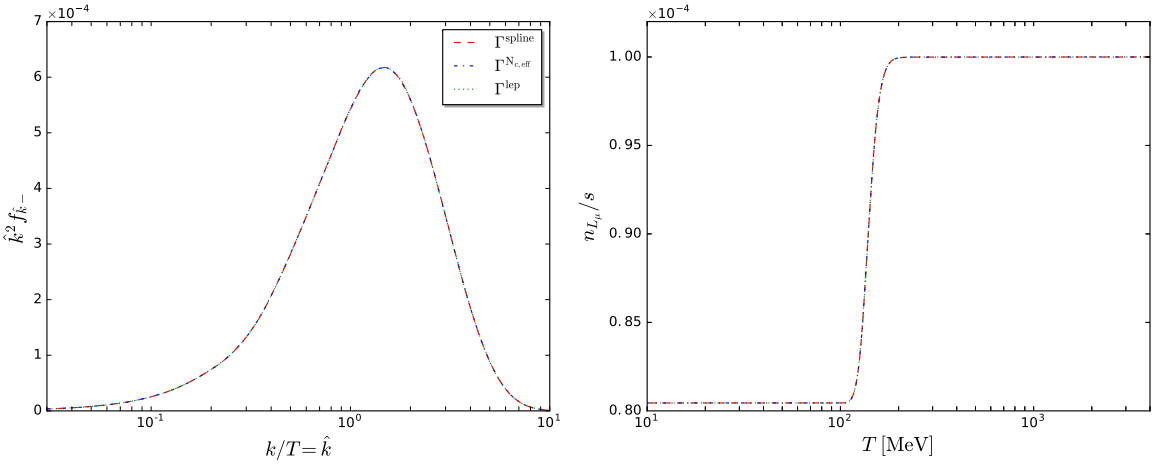
×10⁻⁴
$\hat{k}^2 f_{\hat{k}-}$
Γ^{spline}
$\Gamma^{\mathrm{N_{c,eff}}}$
Γ^{lep}
$k/T = \hat{k}$
×10⁻⁴
n_{L_μ}/s
T [MeV]

Appendix B

Opacity calculation

Here we calculate the opacity (7.10), which we obtain from the imaginary part of the one-loop self-energy diagram shown in figure 4.1 (left), with the scalar field ϕ replacing the gauge boson. In the absence of any chemical potentials, we write the self-energy contribution from interactions with the scalar field ϕ as

$$\Sigma(k) = \not{k} a^\phi - \gamma^0 \left(b^\phi + \frac{i\Gamma^\phi}{2} \right), \tag{B.1}$$

where a^ϕ is usually neglected against the tree-level term when inserting the self-energy into the neutrino propagator (cf. (4.10)). For calculating the self-energy in the first place, we keep all terms. From (B.1), the opacity is extracted as

$$\Gamma^\phi = \frac{1}{2\mathbf{k}^2} \mathrm{Tr} \Big[(k^2 \gamma^0 - \omega \not{k}) \mathrm{Im}\Sigma(k) \Big], \tag{B.2}$$

with the four-momentum $k = (\omega, \mathbf{k})$. Assuming massless neutrinos, we set $|\mathbf{k}| = \omega$ and the first term drops out immediately since $k^2 = 0$.

For the diagram evaluation, we use the imaginary-time formalism of finite-temperature quantum field theory with four-momenta $k = (k^0, \mathbf{k})$, where $k^0 = i\omega_n$ and $\omega_n = \pi n T$ with even (odd) n denoting bosonic (fermionic) Matsubara frequencies. The space-time metric has the signature $(+,-,-,-)$. At one-loop order, the self-energy reads

$$\Sigma(k) = -\lambda^2 \sum\!\!\!\!\!\!\int_p \frac{\not{p} + \not{k}}{(p+k)^2 (p^2 - m_\phi^2)}, \tag{B.3}$$

where the sum-integral contains the three-dimensional integration over spatial momenta and the summation over all frequencies,

$$\sum\!\!\!\!\!\!\int_p \equiv T \sum_n \int \frac{d^3 p}{(2\pi)^3}. \tag{B.4}$$

For calculating the opacity, we take the following steps: we will compute the trace of $\not{k}$ times expression (B.3), carry out the Matsubara sums, analytically continue the frequency k^0 to the real axis, extract the imaginary part from the discontinuity across that axis and finally, handle the spatial integration. With $\mathrm{Tr}[\not{k}\not{p} + k^2] = 4(p \cdot k + k^2) = 2((p+k)^2 - p^2 - m_\phi^2 + m_\phi^2 + k^2)$, we need to compute

$$\mathrm{Tr}[\not{k}\Sigma(k)] = -2\lambda^2 \sum\!\!\!\!\!\!\int_p \left[\frac{1}{p^2 - m_\phi^2} - \frac{1}{(p+k)^2} + \frac{k^2 - m_\phi^2}{(p+k)^2(p^2 - m_\phi^2)}\right]. \tag{B.5}$$

The first two terms are k-independent and thus do not contribute to the discontinuity of k^0 across the real axis. Only the third term contributes to the imaginary part and will be kept. The denominator of that term is handled through partial fraction decomposition,

$$\begin{aligned}\frac{1}{[(p^0+k^0)^2 - E_2^2][p^{0\,2} - E_1^2]} =& \frac{1}{4E_1E_2} \\ &\left[\frac{1}{E_1 - k^0 - E_2}\left(\frac{1}{p^0 + k^0 + E_2} - \frac{1}{p^0 + E_1}\right)\right. \\ &+\frac{1}{E_1 + k^0 + E_2}\left(\frac{1}{p^0 + k^0 + E_2} - \frac{1}{p^0 - E_1}\right) \\ &-\frac{1}{E_1 - k^0 + E_2}\left(\frac{1}{p^0 + k^0 - E_2} - \frac{1}{p^0 + E_1}\right) \\ &\left.-\frac{1}{E_1 + k^0 - E_2}\left(\frac{1}{p^0 + k^0 - E_2} - \frac{1}{p^0 - E_1}\right)\right],\end{aligned} \tag{B.6}$$

with $E_1 = \sqrt{\mathbf{p}^2 + m_\phi^2}$ and $E_2 = |\mathbf{p} + \mathbf{k}|$. This allows us to easily carry out the bosonic Matsubara sums over p^0 (for a general guide on how to solve them, we refer to [106]). We find

$$\begin{aligned}\mathrm{Tr}[\not{k}\Sigma(k)] =& 4\lambda^2 m_\phi^2 \int \frac{d^3p}{(2\pi)^3}\frac{1}{4E_1E_2} \\ &\left[\frac{1}{E_1 - k^0 - E_2}\Big(-f_F - f_B\Big)\right. \\ &+\frac{1}{E_1 + k^0 + E_2}\Big(-f_F + (1+f_B)\Big) \\ &-\frac{1}{E_1 - k^0 + E_2}\Big(-(1-f_F) - f_B\Big) \\ &\left.-\frac{1}{E_1 + k^0 - E_2}\Big(-(1-f_F) + (1+f_B)\Big)\right],\end{aligned} \tag{B.7}$$

with $f_B = f_B(E_1), f_F = f_F(E_2)$. Now we analytically continue $k^0 \to \omega + i0^+$ with real frequency ω and use the identity

$$\frac{1}{x \pm i0^+} = \text{p.v.}\left(\frac{1}{x}\right) \mp i\pi\delta(x) \tag{B.8}$$

to extract the imaginary part. This gives

$$\begin{aligned}\text{Tr}[\not{k}\text{Im}\Sigma(k)] =& \pi\lambda^2 m_\phi^2 \int \frac{d^3p}{(2\pi)^3}\frac{1}{E_1E_2} \\ &\Big[\delta(E_1 - \omega - E_2)\Big(- f_F - f_B\Big) \\ &-\delta(E_1 + \omega + E_2)\Big(- f_F + (1 + f_B)\Big) \\ &-\delta(E_1 - \omega + E_2)\Big(- (1 - f_F) - f_B\Big) \\ &+\delta(E_1 + \omega - E_2)\Big(- (1 - f_F) + (1 + f_B)\Big)\Big].\end{aligned} \tag{B.9}$$

Since the active neutrinos are assumed massless, only the first of the four terms contributes as it is the only kinematically allowed one. Using (B.2), we are left with

$$\Gamma^\phi = \frac{\pi\lambda^2 m_\phi^2}{2\omega}\int \frac{d^3p}{(2\pi)^3}\frac{1}{E_1E_2}\delta(E_1 - \omega - E_2)\Big(f_F(E_2) + f_B(E_1)\Big). \tag{B.10}$$

We denote the integral containing f_F by I_F and handle it as follows. We shift the $\mathbf{k}$-dependence out of the distribution function by substituting $\mathbf{u} = \mathbf{p}+\mathbf{k}$ and renaming $\mathbf{u} \equiv \mathbf{p}$ afterwards, yielding

$$I_F = \int \frac{d^3p}{(2\pi)^3}\frac{f_F(|\mathbf{p}|)}{\sqrt{(\mathbf{p}-\mathbf{k})^2 + m_\phi^2}|\mathbf{p}|}\delta\Big(\sqrt{(\mathbf{p}-\mathbf{k})^2 + m_\phi^2} - \omega - |\mathbf{p}|\Big). \tag{B.11}$$

We continue by substituting $\mathbf{p} - \mathbf{k} = \mathbf{q}$ and inserting a delta distribution, making use of the identity

$$g(\mathbf{p} - \mathbf{k}) = \int d^3q\, \delta^{(3)}(\mathbf{q} - \mathbf{p} + \mathbf{k})g(\mathbf{q}). \tag{B.12}$$

By shifting $\mathbf{q} \to -\mathbf{q}$, $\mathbf{p} \to -\mathbf{p}$ and using the symmetry of the delta distribution, we arrive at

$$I_F = \int \frac{d^3p}{(2\pi)^3}\int \frac{d^3q}{\sqrt{\mathbf{q}^2 + m_\phi^2}|\mathbf{p}|}f_F(|\mathbf{p}|)\delta^{(3)}(\mathbf{q}-\mathbf{p}-\mathbf{k})\delta\Big(\sqrt{\mathbf{q}^2 + m_\phi^2}-\omega-|\mathbf{p}|\Big). \tag{B.13}$$

A useful trick is to promote the momenta p and q to 4-vectors $p = (|\mathbf{p}|, \mathbf{p})$ and $q = (q^0, \mathbf{q})$ with $q^0 = \sqrt{\mathbf{q}^2 + m_\phi^2}$. Then the delta distributions in (B.13) can be combined into a four-dimensional delta distribution, which is used to cancel the Lorentz-invariant expression

$$\int \frac{d^3q}{(2\pi)^3 2q^0} = \int \frac{d^4q}{(2\pi)^3}\delta\big(q^2 - m_\phi^2\big)\theta(q^0). \tag{B.14}$$

This leaves us with

$$I_F = 2\int \frac{d^3p}{(2\pi)^3}\frac{f_F(|\mathbf{p}|)}{|\mathbf{p}|}\delta\big((p+k)^2 - m_\phi^2\big)\theta(\omega + |\mathbf{p}|), \tag{B.15}$$

where we can safely drop the Heaviside function since its argument is always positive. The remaining spatial integral is easily computed in spherical coordinates. We denote by z the cosine of the angle between both vectors, which is chosen as the polar angle. Expanding the argument of the delta distribution then yields

$$\delta\big(2|\mathbf{p}|\omega - 2|\mathbf{p}|\omega z - m_\phi^2\big) = \frac{1}{2|\mathbf{p}|\omega}\delta\Big(\frac{m_\phi^2}{2|\mathbf{p}|\omega} - 1 + z\Big). \tag{B.16}$$

From the lower integration limit on the polar angle, $z \geq -1$, the delta distribution gives the lower limit $|\mathbf{p}| \geq m_\phi^2/(4\omega)$ on the radial coordinate upon integrating over z. For smaller values, it does not contribute. In the end, this gives

$$I_F = \frac{1}{4\pi^2\omega}\int_{\frac{m_\phi^2}{4\omega}}^{\infty} d|\mathbf{p}| f_F(|\mathbf{p}|) = \frac{T}{4\pi^2\omega}\left[\ln\left(1 + e^{m_\phi^2/(4\omega T)}\right) - \frac{m_\phi^2}{4\omega T}\right]. \tag{B.17}$$

Similar steps are made in the computation of the second part of (B.10), containing the integral over the Bose-distribution. This part is denoted by I_B. We find

$$I_B = 2\int \frac{d^3p}{(2\pi)^3}\frac{f_B(p^0)}{p^0}\frac{1}{2|\mathbf{p}|\omega}\delta\Big(\frac{m_\phi^2}{2|\mathbf{p}|\omega} - \frac{p^0}{|\mathbf{p}|} + z\Big)\theta(p^0 - \omega), \tag{B.18}$$

where now $p^0 = \sqrt{\mathbf{p}^2 + m_\phi^2}$. Again, using spherical coordinates, the delta distribution gives constraints on the integration range of $|\mathbf{p}|$. From $z \leq 1$, it follows that $|\mathbf{p}| \geq (4\omega^2 - m_\phi^2)/(4\omega)$, whereas from $z \geq -1$, it follows that $|\mathbf{p}| \geq (m_\phi^2 - 4\omega^2)/(4\omega)$. So the lower integration limit is $|\mathbf{p}| \geq |m_\phi^2 - 4\omega^2|/(4\omega)$. Then we obtain

$$\begin{aligned} I_B &= \frac{1}{4\pi^2\omega}\int_{\frac{|m_\phi^2 - 4\omega^2|}{4\omega}}^{\infty} d|\mathbf{p}|\,\frac{p f_B(p^0)}{p^0}\theta(p^0 - \omega) \\ &= \frac{T}{4\pi^2\omega}\left[\frac{m_\phi^2}{4\omega T} + \frac{\omega}{T} - \ln\left(e^{m_\phi^2/(4\omega T) + \omega/T} - 1\right)\right]. \end{aligned} \tag{B.19}$$

Putting everything together, we arrive at the final result

$$\begin{aligned}\Gamma^{\phi} &= \frac{\pi\lambda^2 m_\phi^2}{2\omega}\Big(I_F + I_B\Big) \\ &= \frac{\lambda^2 m_\phi^2 T}{8\pi\omega^2}\left[\ln\left(1+e^{m_\phi^2/(4\omega T)}\right) + \frac{\omega}{T} - \ln\left(e^{m_\phi^2/(4\omega T)+\omega/T}-1\right)\right],\end{aligned} \tag{B.20}$$

which is given in (7.10) (remembering that $|\mathbf{k}| = \omega$). For comparison, our result coincides with the result of [22] in the limit $I_B = 0$. This holds for large ω.

List of Figures

List of Tables

References

[1] D. Bödeker and A. Klaus, *Sterile neutrino dark matter: Impact of active-neutrino opacities*, *JHEP* **07** (2020) 218, [2005.03039].

[2] A. A. Penzias and R. W. Wilson, *A Measurement of excess antenna temperature at 4080-Mc/s*, *Astrophys. J.* **142** (1965) 419–421.

[3] ATLAS collaboration, G. Aad et al., *Observation of a new particle in the search for the Standard Model Higgs boson with the ATLAS detector at the LHC*, *Phys. Lett. B* **716** (2012) 1–29, [1207.7214].

[4] CMS collaboration, S. Chatrchyan et al., *Observation of a New Boson at a Mass of 125 GeV with the CMS Experiment at the LHC*, *Phys. Lett. B* **716** (2012) 30–61, [1207.7235].

[5] Particle Data Group collaboration, P. Zyla et al., *Review of Particle Physics*, *PTEP* **2020** (2020) 083C01.

[6] Planck collaboration, N. Aghanim et al., *Planck 2018 results. VI. Cosmological parameters*, *Astron. Astrophys.* **641** (2020) A6, [1807.06209].

[7] A. A. Klypin, A. V. Kravtsov, O. Valenzuela and F. Prada, *Where are the missing Galactic satellites?*, *Astrophys. J.* **522** (1999) 82–92, [astro-ph/9901240].

[8] M. Boylan-Kolchin, J. S. Bullock and M. Kaplinghat, *Too big to fail? The puzzling darkness of massive Milky Way subhaloes*, *Mon. Not. Roy. Astron. Soc.* **415** (2011) L40, [1103.0007].

[9] S. D. White, C. Frenk and M. Davis, *Clustering in a Neutrino Dominated Universe*, *Astrophys. J. Lett.* **274** (1983) L1–L5.

[10] M. R. Lovell, V. Eke, C. S. Frenk, L. Gao, A. Jenkins, T. Theuns et al., *The Haloes of Bright Satellite Galaxies in a Warm Dark Matter Universe*, *Mon. Not. Roy. Astron. Soc.* **420** (2012) 2318–2324, [1104.2929].

[11] S. Dodelson and L. M. Widrow, *Sterile-neutrinos as dark matter*, *Phys. Rev. Lett.* **72** (1994) 17–20, [hep-ph/9303287].

[12] U. Seljak, A. Makarov, P. McDonald and H. Trac, *Can sterile neutrinos be the dark matter?*, *Phys. Rev. Lett.* **97** (2006) 191303, [astro-ph/0602430].

[13] A. Boyarsky, O. Ruchayskiy and M. Shaposhnikov, *The Role of sterile neutrinos in cosmology and astrophysics*, *Ann. Rev. Nucl. Part. Sci.* **59** (2009) 191–214, [0901.0011].

[14] A. Boyarsky, J. Lesgourgues, O. Ruchayskiy and M. Viel, *Lyman-alpha constraints on warm and on warm-plus-cold dark matter models*, *JCAP* **0905** (2009) 012, [0812.0010].

[15] X.-D. Shi and G. M. Fuller, *A New dark matter candidate: Nonthermal sterile neutrinos*, *Phys. Rev. Lett.* **82** (1999) 2832–2835, [astro-ph/9810076].

[16] K. Kainulainen, *Light Singlet Neutrinos and the Primordial Nucleosynthesis*, *Phys. Lett. B* **244** (1990) 191–195.

[17] P. G. Langacker, *On the cosmological production of light sterile neutrinos*, Tech. Rep. UPR-0401-T, Pennsylvania Univ. Dept. Phys., Philadelphia, PA, Sep, 1989.

[18] A. Dolgov and S. Hansen, *Massive sterile neutrinos as warm dark matter*, *Astropart. Phys.* **16** (2002) 339–344, [hep-ph/0009083].

[19] K. Abazajian, G. M. Fuller and M. Patel, *Sterile neutrino hot, warm, and cold dark matter*, *Phys. Rev.* **D64** (2001) 023501, [astro-ph/0101524].

[20] Y. Aoki, G. Endrodi, Z. Fodor, S. Katz and K. Szabo, *The Order of the quantum chromodynamics transition predicted by the standard model of particle physics*, *Nature* **443** (2006) 675–678, [hep-lat/0611014].

[21] T. Bhattacharya et al., *QCD Phase Transition with Chiral Quarks and Physical Quark Masses*, *Phys. Rev. Lett.* **113** (2014) 082001, [1402.5175].

[22] A. De Gouvêa, M. Sen, W. Tangarife and Y. Zhang, *Dodelson-Widrow Mechanism in the Presence of Self-Interacting Neutrinos*, *Phys. Rev. Lett.* **124** (2020) 081802, [1910.04901].

[23] F. Zwicky, *Die Rotverschiebung von extragalaktischen Nebeln*, *Helv. Phys. Acta* **6** (1933) 110–127.

[24] V. C. Rubin and J. Ford, W.Kent, *Rotation of the Andromeda Nebula from a Spectroscopic Survey of Emission Regions*, *Astrophys. J.* **159** (1970) 379–403.

[25] K. Begeman, A. Broeils and R. Sanders, *Extended rotation curves of spiral galaxies: Dark haloes and modified dynamics*, *Mon. Not. Roy. Astron. Soc.* **249** (1991) 523.

[26] H. Hoekstra and B. Jain, *Weak Gravitational Lensing and its Cosmological Applications*, *Ann. Rev. Nucl. Part. Sci.* **58** (2008) 99–123, [0805.0139].

[27] D. Clowe, M. Bradac, A. H. Gonzalez, M. Markevitch, S. W. Randall, C. Jones et al., *A direct empirical proof of the existence of dark matter*, *Astrophys. J. Lett.* **648** (2006) L109–L113, [astro-ph/0608407].

[28] M. Markevitch, A. Gonzalez, D. Clowe, A. Vikhlinin, L. David, W. Forman et al., *Direct constraints on the dark matter self-interaction cross-section from the merging galaxy cluster 1E0657-56*, *Astrophys. J.* **606** (2004) 819–824, [astro-ph/0309303].

[29] https://chandra.harvard.edu/photo/2006/1e0657/more.html Credit: X-ray: NASA/CXC/CfA/ M.Markevitch et al.; Lensing Map: NASA/STScI; ESO WFI; Magellan/U.Arizona/ D.Clowe et al. Optical: NASA/STScI; Magellan/U.Arizona/D.Clowe et al.

[30] W. Hu, N. Sugiyama and J. Silk, *The Physics of microwave background anisotropies*, *Nature* **386** (1997) 37–43, [astro-ph/9604166].

[31] https://www.esa.int/ESA_Multimedia/Images/2013/03/Planck_Power_Spectrum Credit goes to ESA and the Planck Collaboration.

[32] S. S. McGaugh and W. de Blok, *Testing the hypothesis of modified dynamics with low surface brightness galaxies and other evidence*, *Astrophys. J.* **499** (1998) 66–81, [astro-ph/9801102].

[33] J. R. Ellis, J. Hagelin, D. V. Nanopoulos, K. A. Olive and M. Srednicki, *Supersymmetric Relics from the Big Bang*, *Nucl. Phys. B* **238** (1984) 453–476.

[34] I. Antoniadis, *A Possible new dimension at a few TeV*, *Phys. Lett. B* **246** (1990) 377–384.

[35] B. Carr, F. Kühnel and M. Sandstad, *Primordial Black Holes as Dark Matter*, *Phys. Rev. D* **94** (2016) 083504, [1607.06077].

[36] T. D. Brandt, *Constraints on MACHO Dark Matter from Compact Stellar Systems in Ultra-Faint Dwarf Galaxies*, *Astrophys. J. Lett.* **824** (2016) L31, [1605.03665].

[37] B. W. Lee and S. Weinberg, *Cosmological Lower Bound on Heavy Neutrino Masses*, *Phys. Rev. Lett.* **39** (1977) 165–168.

[38] G. Jungman, M. Kamionkowski and K. Griest, *Supersymmetric dark matter*, *Phys. Rept.* **267** (1996) 195–373, [hep-ph/9506380].

[39] R. Peccei and H. R. Quinn, *CP Conservation in the Presence of Instantons*, *Phys. Rev. Lett.* **38** (1977) 1440–1443.

[40] J. M. Pendlebury et al., *Revised experimental upper limit on the electric dipole moment of the neutron*, *Phys. Rev. D* **92** (2015) 092003, [1509.04411].

[41] M. S. Turner, *Thermal Production of Not SO Invisible Axions in the Early Universe*, *Phys. Rev. Lett.* **59** (1987) 2489.

[42] S. Hannestad, A. Mirizzi, G. G. Raffelt and Y. Y. Wong, *Neutrino and axion hot dark matter bounds after WMAP-7*, *JCAP* **08** (2010) 001, [1004.0695].

[43] R. L. Davis, *Cosmic Axions from Cosmic Strings*, *Phys. Lett. B* **180** (1986) 225–230.

[44] S. Chang, C. Hagmann and P. Sikivie, *Studies of the motion and decay of axion walls bounded by strings*, *Phys. Rev. D* **59** (1999) 023505, [hep-ph/9807374].

[45] J. Preskill, M. B. Wise and F. Wilczek, *Cosmology of the Invisible Axion*, *Phys. Lett. B* **120** (1983) 127–132.

[46] L. Abbott and P. Sikivie, *A Cosmological Bound on the Invisible Axion*, *Phys. Lett. B* **120** (1983) 133–136.

[47] M. Dine and W. Fischler, *The Not So Harmless Axion*, *Phys. Lett. B* **120** (1983) 137–141.

[48] A. Coc, J.-P. Uzan and E. Vangioni, *Standard big bang nucleosynthesis and primordial CNO Abundances after Planck*, *JCAP* **10** (2014) 050, [1403.6694].

[49] A. Sakharov, *Violation of CP Invariance, C asymmetry, and baryon asymmetry of the universe*, *Pisma Zh.Eksp.Teor.Fiz.* **5** (1967) 32–35.

[50] G. 't Hooft, *Symmetry Breaking Through Bell-Jackiw Anomalies*, *Phys. Rev. Lett.* **37** (1976) 8–11.

[51] F. R. Klinkhamer and N. Manton, *A Saddle Point Solution in the Weinberg-Salam Theory*, *Phys. Rev. D* **30** (1984) 2212.

[52] M. Gavela, P. Hernandez, J. Orloff and O. Pene, *Standard model CP violation and baryon asymmetry*, *Mod. Phys. Lett. A* **9** (1994) 795–810, [hep-ph/9312215].

[53] M. Gavela, P. Hernandez, J. Orloff, O. Pene and C. Quimbay, *Standard model CP violation and baryon asymmetry. Part 2: Finite temperature*, *Nucl. Phys. B* **430** (1994) 382–426, [hep-ph/9406289].

[54] V. Kuzmin, V. Rubakov and M. Shaposhnikov, *On the Anomalous Electroweak Baryon Number Nonconservation in the Early Universe*, *Phys. Lett. B* **155** (1985) 36.

[55] K. Kajantie, M. Laine, K. Rummukainen and M. E. Shaposhnikov, *Is there a hot electroweak phase transition at m(H) larger or equal to m(W)?*, *Phys. Rev. Lett.* **77** (1996) 2887–2890, [hep-ph/9605288].

[56] M. Fukugita and T. Yanagida, *Baryogenesis Without Grand Unification*, *Phys. Lett. B* **174** (1986) 45–47.

[57] A. Pilaftsis and T. E. Underwood, *Resonant leptogenesis*, *Nucl. Phys. B* **692** (2004) 303–345, [hep-ph/0309342].

[58] E. K. Akhmedov, V. Rubakov and A. Smirnov, *Baryogenesis via neutrino oscillations*, *Phys. Rev. Lett.* **81** (1998) 1359–1362, [hep-ph/9803255].

[59] J. D. Simon and M. Geha, *The Kinematics of the Ultra-Faint Milky Way Satellites: Solving the Missing Satellite Problem*, *Astrophys. J.* **670** (2007) 313–331, [0706.0516].

[60] J. Alvey, N. Sabti, V. Tiki, D. Blas, K. Bondarenko, A. Boyarsky et al., *New Constraints on the Mass of Fermionic Dark Matter from Dwarf Spheroidal Galaxies*, 2010.03572.

[61] S. Tremaine and J. E. Gunn, *Dynamical Role of Light Neutral Leptons in Cosmology*, *Phys. Rev. Lett.* **42** (1979) 407–410.

[62] T. Venumadhav, F.-Y. Cyr-Racine, K. N. Abazajian and C. M. Hirata, *Sterile neutrino dark matter: Weak interactions in the strong coupling epoch*, *Phys. Rev.* **D94** (2016) 043515, [1507.06655].

[63] J. Ghiglieri and M. Laine, *Improved determination of sterile neutrino dark matter spectrum*, *JHEP* **11** (2015) 171, [1506.06752].

[64] A. Boyarsky, O. Ruchayskiy and D. Iakubovskyi, *A Lower bound on the mass of Dark Matter particles*, *JCAP* **0903** (2009) 005, [0808.3902].

[65] K. Abazajian, G. M. Fuller and W. H. Tucker, *Direct detection of warm dark matter in the X-ray*, *Astrophys. J.* **562** (2001) 593–604, [astro-ph/0106002].

[66] P. B. Pal and L. Wolfenstein, *Radiative Decays of Massive Neutrinos*, *Phys. Rev. D* **25** (1982) 766.

[67] S. Riemer-Sorensen, S. H. Hansen and K. Pedersen, *Sterile neutrinos in the Milky Way: Observational constraints*, *Astrophys. J.* **644** (2006) L33–L36, [astro-ph/0603661].

[68] O. Ruchayskiy, A. Boyarsky, D. Iakubovskyi, E. Bulbul, D. Eckert, J. Franse et al., *Searching for decaying dark matter in deep XMM–Newton observation of the Draco dwarf spheroidal*, *Mon. Not. Roy. Astron. Soc.* **460** (2016) 1390–1398, [1512.07217].

[69] B. M. Roach, K. C. Ng, K. Perez, J. F. Beacom, S. Horiuchi, R. Krivonos et al., *NuSTAR Tests of Sterile-Neutrino Dark Matter: New Galactic Bulge Observations and Combined Impact*, *Phys. Rev. D* **101** (2020) 103011, [1908.09037].

[70] A. Boyarsky, D. Malyshev, A. Neronov and O. Ruchayskiy, *Constraining DM properties with SPI*, *Mon. Not. Roy. Astron. Soc.* **387** (2008) 1345, [0710.4922].

[71] E. Bulbul, M. Markevitch, A. Foster, R. K. Smith, M. Loewenstein and S. W. Randall, *Detection of An Unidentified Emission Line in the Stacked X-ray spectrum of Galaxy Clusters*, *Astrophys. J.* **789** (2014) 13, [1402.2301].

[72] A. Boyarsky, O. Ruchayskiy, D. Iakubovskyi and J. Franse, *Unidentified Line in X-Ray Spectra of the Andromeda Galaxy and Perseus Galaxy Cluster*, *Phys. Rev. Lett.* **113** (2014) 251301, [1402.4119].

[73] T. E. Jeltema and S. Profumo, *Discovery of a 3.5 keV line in the Galactic Centre and a critical look at the origin of the line across astronomical targets*, *Mon. Not. Roy. Astron. Soc.* **450** (2015) 2143–2152, [1408.1699].

[74] R. Adhikari, M. Agostini, N. A. Ky, T. Araki, M. Archidiacono, M. Bahr et al., *A white paper on keV sterile neutrino dark matter*, *Journal of Cosmology and Astroparticle Physics* **2017** (jan, 2017) 025–025.

[75] K. Petraki and A. Kusenko, *Dark-matter sterile neutrinos in models with a gauge singlet in the Higgs sector*, *Phys. Rev. D* **77** (2008) 065014, [0711.4646].

[76] F. Bezrukov, H. Hettmansperger and M. Lindner, *keV sterile neutrino Dark Matter in gauge extensions of the Standard Model*, *Phys. Rev. D* **81** (2010) 085032, [0912.4415].

[77] V. Vipp, A. Hektor and G. Hütsi, *Rapid onset of the 21-cm signal suggests a preferred mass range for dark matter particle*, 2103.07462.

[78] A. Boyarsky, D. Iakubovskyi and O. Ruchayskiy, *Next decade of sterile neutrino studies*, *Phys. Dark Univ.* **1** (2012) 136–154, [1306.4954].

[79] N. Palanque-Delabrouille, C. Yèche, N. Schöneberg, J. Lesgourgues, M. Walther, S. Chabanier et al., *Hints, neutrino bounds and WDM constraints from SDSS DR14 Lyman-α and Planck full-survey data*, *JCAP* **04** (2020) 038, [1911.09073].

[80] S. S. Gershtein and Y. B. Zeldovich, *Rest Mass of Muonic Neutrino and Cosmology*, *JETP Lett.* **4** (1966) 120–122.

[81] R. Cowsik and J. McClelland, *An Upper Limit on the Neutrino Rest Mass*, *Phys. Rev. Lett.* **29** (1972) 669–670.

[82] S. Colombi, S. Dodelson and L. M. Widrow, *Large scale structure tests of warm dark matter*, *Astrophys. J.* **458** (1996) 1, [astro-ph/9505029].

[83] V. Iršič et al., *New Constraints on the free-streaming of warm dark matter from intermediate and small scale Lyman-α forest data*, *Phys. Rev. D* **96** (2017) 023522, [1702.01764].

[84] S. P. Mikheyev and A. Y. Smirnov, *Resonance Amplification of Oscillations in Matter and Spectroscopy of Solar Neutrinos*, *Sov. J. Nucl. Phys.* **42** (1985) 913–917.

[85] L. Wolfenstein, *Neutrino Oscillations in Matter*, *Phys. Rev. D* **17** (1978) 2369–2374.

[86] G. Steigman, *Primordial Nucleosynthesis in the Precision Cosmology Era*, *Ann. Rev. Nucl. Part. Sci.* **57** (2007) 463–491, [0712.1100].

[87] P. D. Serpico and G. G. Raffelt, *Lepton asymmetry and primordial nucleosynthesis in the era of precision cosmology*, *Phys. Rev. D* **71** (2005) 127301, [astro-ph/0506162].

[88] I. M. Oldengott and D. J. Schwarz, *Improved constraints on lepton asymmetry from the cosmic microwave background*, *EPL* **119** (2017) 29001, [1706.01705].

[89] C. Pitrou, A. Coc, J.-P. Uzan and E. Vangioni, *Precision big bang nucleosynthesis with improved Helium-4 predictions*, *Phys. Rept.* **754** (2018) 1–66, [1801.08023].

[90] V. A. Rubakov and D. S. Gorbunov, *Introduction to the Theory of the Early Universe: Hot big bang theory*. World Scientific, Singapore, 2017, 10.1142/10447.

[91] L. Husdal, *On Effective Degrees of Freedom in the Early Universe*, *Galaxies* **4** (2016) 78, [1609.04979].

[92] Y. Izotov and T. Thuan, *Systematic effects and a new determination of the primordial abundance of He-4 and dY/dZ from observations of blue compact galaxies*, *Astrophys. J.* **602** (2004) 200–230, [astro-ph/0310421].

[93] R. K. Sachs and A. M. Wolfe, *Perturbations of a cosmological model and angular variations of the microwave background*, *Astrophys. J.* **147** (1967) 73–90.

[94] M. Laine and Y. Schröder, *Quark mass thresholds in QCD thermodynamics*, *Phys. Rev.* **D73** (2006) 085009, [hep-ph/0603048].

[95] M. D'Onofrio, K. Rummukainen and A. Tranberg, *Sphaleron Rate in the Minimal Standard Model*, *Phys. Rev. Lett.* **113** (2014) 141602, [1404.3565].

[96] HotQCD collaboration, P. Steinbrecher, *The QCD crossover at zero and non-zero baryon densities from Lattice QCD*, *Nucl. Phys. A* **982** (2019) 847–850, [1807.05607].

[97] T. Asaka, M. Laine and M. Shaposhnikov, *Lightest sterile neutrino abundance within the nuMSM*, *JHEP* **01** (2007) 091, [hep-ph/0612182].

[98] HotQCD collaboration, A. Bazavov et al., *Fluctuations and Correlations of net baryon number, electric charge, and strangeness: A comparison of lattice QCD results with the hadron resonance gas model*, *Phys. Rev.* **D86** (2012) 034509, [1203.0784].

[99] S. Borsányi, Z. Fodor, S. D. Katz, S. Krieg, C. Ratti and K. Szabó, *Fluctuations of conserved charges at finite temperature from lattice QCD*, *JHEP* **01** (2012) 138, [1112.4416].

[100] T. Asaka, M. Laine and M. Shaposhnikov, *On the hadronic contribution to sterile neutrino production*, *JHEP* **06** (2006) 053, [hep-ph/0605209].

[101] J. Ghiglieri and M. Laine, *Sterile neutrino dark matter via GeV-scale leptogenesis?*, *JHEP* **07** (2019) 078, [1905.08814].

[102] D. Bödeker and D. Schröder, *Kinetic equations for sterile neutrinos from thermal fluctuations*, *JCAP* **02** (2020) 033, [1911.05092].

[103] H. A. Weldon, *Effective Fermion Masses of Order gT in High Temperature Gauge Theories with Exact Chiral Invariance*, *Phys. Rev.* **D26** (1982) 2789.

[104] D. Nötzold and G. Raffelt, *Neutrino Dispersion at Finite Temperature and Density*, *Nucl. Phys.* **B307** (1988) 924–936.

[105] M. L. Bellac, *Thermal Field Theory*. Cambridge Monographs on Mathematical Physics. Cambridge University Press, 3, 2011, 10.1017/CBO9780511721700.

[106] M. Laine and A. Vuorinen, *Basics of Thermal Field Theory*, vol. 925. Springer, 2016, 10.1007/978-3-319-31933-9.

[107] R. Essig, E. Kuflik, S. D. McDermott, T. Volansky and K. M. Zurek, *Constraining Light Dark Matter with Diffuse X-Ray and Gamma-Ray Observations*, *JHEP* **11** (2013) 193, [1309.4091].

[108] S. Horiuchi, P. J. Humphrey, J. Onorbe, K. N. Abazajian, M. Kaplinghat and S. Garrison-Kimmel, *Sterile neutrino dark matter bounds from galaxies of the Local Group*, *Phys. Rev.* **D89** (2014) 025017, [1311.0282].

[109] K. Perez, K. C. Y. Ng, J. F. Beacom, C. Hersh, S. Horiuchi and R. Krivonos, *Almost closing the νMSM sterile neutrino dark matter window with NuSTAR*, *Phys. Rev.* **D95** (2017) 123002, [1609.00667].

[110] K. C. Y. Ng, B. M. Roach, K. Perez, J. F. Beacom, S. Horiuchi, R. Krivonos et al., *New Constraints on Sterile Neutrino Dark Matter from NuSTAR M31 Observations*, *Phys. Rev.* **D99** (2019) 083005, [1901.01262].

[111] T. Asaka, S. Blanchet and M. Shaposhnikov, *The nuMSM, dark matter and neutrino masses*, *Phys. Lett. B* **631** (2005) 151–156, [hep-ph/0503065].

[112] M. Shaposhnikov, *The nuMSM, leptonic asymmetries, and properties of singlet fermions*, *JHEP* **08** (2008) 008, [0804.4542].

[113] M. Laine and M. Shaposhnikov, *Sterile neutrino dark matter as a consequence of nuMSM-induced lepton asymmetry*, *JCAP* **0806** (2008) 031, [0804.4543].

[114] J. Ghiglieri and M. Laine, *Precision study of GeV-scale resonant leptogenesis*, *JHEP* **02** (2019) 014, [1811.01971].

[115] J. F. Cherry and S. Horiuchi, *Closing in on Resonantly Produced Sterile Neutrino Dark Matter*, *Phys. Rev.* **D95** (2017) 083015, [1701.07874].

[116] A. Schneider, *Astrophysical constraints on resonantly produced sterile neutrino dark matter*, *JCAP* **1604** (2016) 059, [1601.07553].

[117] A. Caputo, M. Regis and M. Taoso, *Searching for Sterile Neutrino with X-ray Intensity Mapping*, *JCAP* **03** (2020) 001, [1911.09120].

[118] A. Boyarsky, M. Drewes, T. Lasserre, S. Mertens and O. Ruchayskiy, *Sterile Neutrino Dark Matter*, *Prog. Part. Nucl. Phys.* **104** (2019) 1–45, [1807.07938].

[119] J. Baur, N. Palanque-Delabrouille, C. Yeche, A. Boyarsky, O. Ruchayskiy, E. Armengaud et al., *Constraints from Ly-α forests on non-thermal dark matter including resonantly-produced sterile neutrinos*, *JCAP* **12** (2017) 013, [1706.03118].

[120] M. Drewes and J. U. Kang, *Sterile neutrino Dark Matter production from scalar decay in a thermal bath*, *JHEP* **05** (2016) 051, [1510.05646].

[121] K. J. Kelly, M. Sen, W. Tangarife and Y. Zhang, *Origin of sterile neutrino dark matter via secret neutrino interactions with vector bosons*, *Phys. Rev. D* **101** (2020) 115031, [2005.03681].

[122] C. Quimbay and S. Vargas-Castrillon, *Fermionic dispersion relations in the standard model at finite temperature*, *Nucl. Phys. B* **451** (1995) 265–304, [hep-ph/9504410].

[123] B. Dasgupta and J. Kopp, *Cosmologically Safe eV-Scale Sterile Neutrinos and Improved Dark Matter Structure*, *Phys. Rev. Lett.* **112** (2014) 031803, [1310.6337].

[124] Y. S. Jeong, S. Palomares-Ruiz, M. H. Reno and I. Sarcevic, *Probing secret interactions of eV-scale sterile neutrinos with the diffuse supernova neutrino background*, *JCAP* **06** (2018) 019, [1803.04541].

[125] N. Blinov, K. J. Kelly, G. Z. Krnjaic and S. D. McDermott, *Constraining the Self-Interacting Neutrino Interpretation of the Hubble Tension*, *Phys. Rev. Lett.* **123** (2019) 191102, [1905.02727].

[126] G.-y. Huang, T. Ohlsson and S. Zhou, *Observational Constraints on Secret Neutrino Interactions from Big Bang Nucleosynthesis*, *Phys. Rev. D* **97** (2018) 075009, [1712.04792].

[127] M. Escudero and S. J. Witte, *A CMB search for the neutrino mass mechanism and its relation to the Hubble tension*, *Eur. Phys. J. C* **80** (2020) 294, [1909.04044].

[128] E949 collaboration, A. V. Artamonov et al., *Search for the rare decay $K^+ \to \mu^+ \nu \bar{\nu} \nu$*, *Phys. Rev. D* **94** (2016) 032012, [1606.09054].

Acknowledgements

First and foremost, I want to thank my supervisor Prof. Dr. Dietrich Bödeker for guiding me through my research project during the last couple of years. Not only having the possibility to always discuss with him and ask for advice but also being asked the right questions is what drove me towards my goals.
I also thank Prof. Dr. Dominik J. Schwarz for evaluating this thesis as the second referee.
Furthermore, I thank Gudrun Eickmeyer, Irene Kehler and Susi v. Reder for all the administrative support.
I am very grateful to all my colleagues and office mates, without whom none of my time as a PhD student would have been even half as interesting and fun as it was. My special thanks goes to Mandy Middeldorf and Dennis Schröder, who I had the pleasure to learn a lot from while discussing and drinking coffee with. More special thanks goes to Patric Hölscher, Pascal Kreling and Hendrik Roch for many interesting and fruitful discussions during the time we shared an office. I also thank Hendrik for proofreading my thesis.
Last but not least, I acknowledge support from the CRC TR-211 'Strong-interaction matter under extreme conditions' and I thank all members for many informative and interesting discussions and colloquia.